Flow Turbulence Combust (2019) 102:89–116
https://doi.org/10.1007/s10494-017-9876-0

A Hierarchical Numerical Journey Through the Nasal Cavity: from Nose-Like Models to Real Anatomies

Andreas Lintermann[1,2] · **Wolfgang Schröder**[1,2]

Received: 29 April 2017 / Accepted: 8 November 2017 / Published online: 20 December 2017

Abstract The immense increase of computational power in the past decades led to an evolution of numerical simulations in all kind of engineering applications. New developments in medical technologies in rhinology employ computational fluid dynamics methods to explore pathologies from a fluid-mechanics point of view. Such methods have grown mature and are about to enter daily clinical use to support doctors in decision making. In light of the importance of effective respiration on patient comfort and health care costs, individualized simulations ultimately have the potential to revolutionize medical diagnosis, drug delivery, and surgery planning. The present article reviews experiments, simulations, and algorithmic approaches developed at RWTH Aachen University that have evolved from fundamental physical analyses using nose-like models to patient-individual analyses based on realistic anatomies and high resolution computations in hierarchical manner.

Keywords Nasal cavity flows · Particle-image velocimetry · Finite volume method · Lattice-Boltzmann method · High performance computing

1 Introduction

Respiration is an essential physiological functionality of the human organism and is responsible for supplying the body with oxygen. The airway consists of the upper and lower airways separated by the larynx. A part of the upper airway is depicted in Fig. 1. The nasal cavity is responsible for olfaction and degustation, filtering fine dust from the air as well as

✉ Andreas Lintermann
A.Lintermann@aia.rwth-aachen.de

[1] Institute of Aerodynamics, RWTH Aachen University, Wüllnerstr. 5a, 52062 Aachen, Germany

[2] Jülich Aachen Research Alliance, High Performance Computing (JARA-HPC), RWTH Aachen University, Seffenter Weg 23, 52074 Aachen, Germany

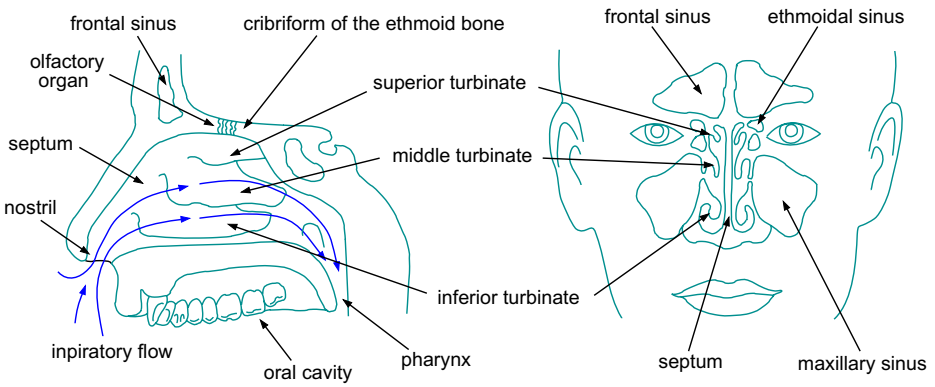

Fig. 1 Schematic side and front view of the anatomy of the human nasal cavity. Inspiratory flow is colored in blue

moisturizing and tempering the air. Therefore, the air is guided past the lower, center, and upper turbinates in the left and right nasal cavity before the cavities unite in the pharynx. Subsequently, the air passes the suppository, oropharynx, epiglottis, and enters the larynx. In the lower airway the larynx is responsible for phonation which is also supported by the paranasal and forehead sinuses. The trachea guides the air towards the left and right main bronchus, which continue to branch out into the bronchioles and finally end with the alveols at the 23rd branching generation.

Obviously, the nasal cavity is indispensable in respiration and a degradation of only one or few functionalities leads to discomfort or further pathologies [1–3]. Such degradations can be the consequence of, e.g., septum deviations, septum perforations, turbinate malformations, chronic rhinosinusitis, swollen turbinates, allergic reactions, or adenoids. Surgery is key to alleviate patient complaints. However, the success rate of rhinological interventions like functional endoscopic sinus surgery (FESS) [4], septoplasty [5], and turbinectomy [6] is often low due to the unpredictability of the effect of anatomical changes on the physical properties of respiration and accompanying side effects [7–10]. To enhance this situation, computational fluid dynamics (CFD) methods enable to numerically predict the flow in the nasal cavity under varying respiration conditions pre- and post-surgically for individual anatomies and pathologies. The integration of such a simulation tool into clinical applications can finally lead to an enhancement of computer-assisted surgery (CAS) [11] by allowing on the one hand, to understand the highly complex flow in intricate nasal geometries and on the other hand, to derive criteria to improve surgery planning.

Many simulation approaches have been followed to understand the flow in the human nasal cavity. These approaches can be categorized by the anatomical models used for the simulations and the applied numerical methods. Hörschler et al. [12–16], Naftali et al. [17, 18], and Finck et al. [19] investigated the flow in nose-like models. Unlike these studies, the investigations in [20–35] considered the flow in anatomically correct in-silico models of nasal cavities. In several of these investigations the Reynolds-averaged Navier-Stokes (RANS) equations were solved by employing one or several turbulence models [21–23, 36] like the k-ω [37], k-ω shear-stress transport (SST) [38], or the k-ϵ [39] model. It should be noted that RANS simulations are based on a fully turbulent flow assumption, whereas the flow in the nasal cavity is mostly in the laminar or transitional regime [13, 19, 26]. The application of such computations is often justified by the value of the REYNOLDS number

which is based on the hydraulic diameter. This is, however, too rough an indicator for such intricate internal flows. Nevertheless, it is fair to state that RANS-based simulations seem to provide reasonable integral results only under certain conditions since turbulence models were developed for different flow regimes. In contrast, large-eddy simulations (LES) solve the temporally and spatially filtered Navier-Stokes equations and make use of subgrid-scale models (SGS) like the Smagorinsky SGS [40] to model high-fidelity flow structures. Finck et al. [19] and Calmet et al. [31] used such LES computations to analyze the flow in a nose-like model of the nasal cavity and in the whole respiratory tract down to the third lung generation. On the other hand, the simulations in [12–16, 20, 24–30, 32–35] solved the governing equations directly, i.e., they performed direct numerical simulations (DNS) which can be assumed to be the most accurate method in case the mesh resolution is sufficient. From a solution method point of view the aforementioned investigations made either use of finite element methods (FEM) [17, 21–23, 31, 33, 34], finite volume methods (FVM) [12–16, 18, 20, 29, 30], or lattice-Boltzmann methods (LBM) [19, 24–28, 32, 35].

The developments and progresses presented in this article, which is a summary of the results presented in [12–16, 24–28, 35, 41], follow the DNS approach. All methods and results hierarchically and consecutively build up on one another. That is, findings from simulations using a FVM and LBM for nose-like to real patient-specific geometries are discussed. For completeness, the discussion of the results is complemented by experimental findings. The investigations have been performed within the frame of a research project that was funded by the German Research Foundation (DFG). This highly interdisciplinary project involved experts from rhinology from the University of Cologne, radiologists from the University Hospital Aachen, and computer scientists and engineers from RWTH Aachen University.

This article possesses the following structure. In Section 2 the hierarchical approach for the experimental and numerical methods for the analysis of nasal cavity flows are sketched. Subsequently, the results are discussed in Section 3 before in Section 4 a summary and an outlook are given.

2 Material and Methods

This section discusses the experimental setup and numerical approaches for the investigations of the flow in nose-like and real anatomies. In the following, the experimental setup will be discussed in Section 2.1. In order to simulate the flow in the human nasal cavity a simulation pipeline has to be traversed. This pipeline consists of the acquisition of an anatomical model for the simulation (Section 2.2), the generation of a computational mesh (Section 2.3), and the numerical simulation (Section 2.4). These steps will be explained in view of advancing technical and algorithmic developments. Note that nose-like models that were investigated in [12–16, 19] are referred to as $\mathcal{G}_{nl}$ (see e.g. Figs. 2 and 3a). Investigations in geometries based on real patient data [24–28, 35] are labeled $\mathcal{G}_r$. An example of such a geometry is shown in Fig. 3b.

2.1 Experimental setup

The sketch in Fig. 2 shows the setup for the experimental investigations of the flow in nose-like models. For the measurements, 3:1 silicone models of the nasal cavity are generated from rapid-prototyped positive nose models and placed in a flow loop with water/glycerol as carrier medium. The silicone features a refractive index which matches that of a volume

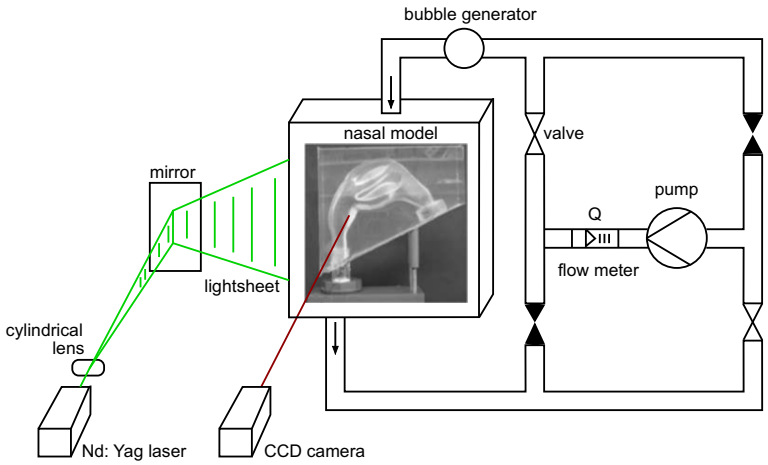

Fig. 2 Principle sketch of the PIV setup and the optical arrangement for measurements in saggital planes parallel to the septum

ratio mixture of glycerol to water of 55%. The complete model is fully immersed in a squared basin made of acrylic glass. At the nostril and the pharynx smooth nozzles are attached that connect to the container box and to the flow loop. The REYNOLDS number is adjusted by adapting the mass flux via a pump. In- and expiration are realized by switching the flow direction. Fine air bubbles are produced by the hydrogen bubble technique and used as tracer particles for particle-image velocimetry (PIV) measurements [42], i.e, particles are illuminated by laser sheets parallel to the septum and are recorded by a charge-coupled device (CCD) camera. The laser sheets are generated by a double pulse Nd:YAG laser. For the measurements 20 saggital and 10 coronal planes with a distance of 1 mm are used. The optical setup corresponds to that employed in [43]. That is, a CCD-video camera with a resolution of 768 $\times$ 512 pixels connected to a S-VHS recorder is used to capture the flow field at a frequency of $f = 25\ Hz$ in interlaced mode. The video is then frame-by-frame digitized and missing lines are interpolated. To allow for a sufficient resolution, the measurements are performed at 5 sections of the model and the results are joined together. For the reconstruction of the velocity vectors a pixel window of 24$\times$24 pixels with a window overlap of 25% is used, resulting in a resolution of $\delta x \approx 1.9\ mm$. The flow is laminar and hence, the resolution is sufficient to capture the important flow features.

2.2 Geometry acquisition

The original data for geometry acquisition stems from computer tomography (CT) images that provide a three-dimensional density field of a scanned object. The range of these values is defined via the Hounsfield scale

$$\Psi = \frac{\mu_m - \mu_w}{\mu_w} \cdot 1,000\ \mathcal{HU}, \tag{1}$$

where μ_m and μ_w are the weakening coefficients of the biological material and water. In general, $\Psi \in [\pm 1,000]\ \mathcal{HU}$ and the interface between air and tissue can be found at around $\Psi_i \in [-400, -200]\ \mathcal{HU}$.

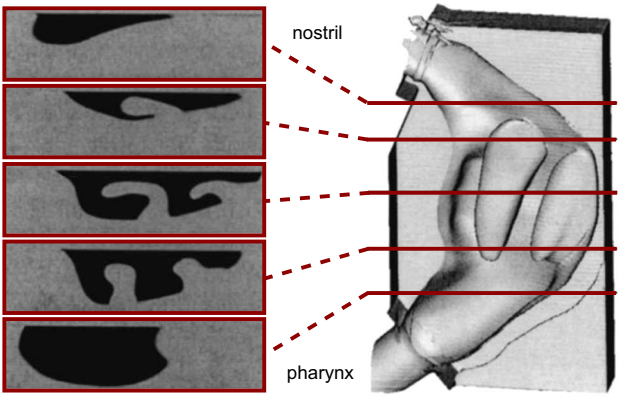

(a)

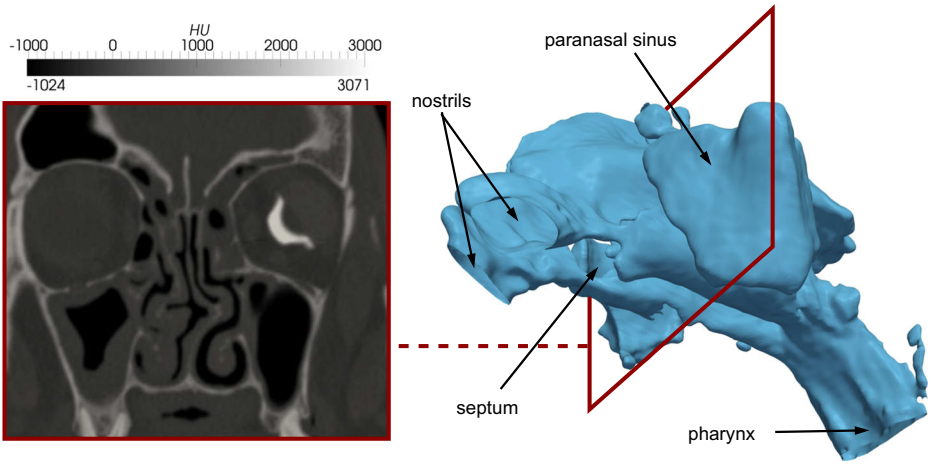

(b)

Fig. 3 Nose-like model and in-silico model of the nasal cavity. **a** CT cross-sections of a nose-like model used for experimental investigations. **b** Real patient CT cross-section and the extracted surface of the nasal cavity

The CT data $\mathcal{C}_{nl}$ for nose-like models $\mathcal{G}_{nl}$ originated from a silicon cast [44] and consisted of 300 slices with a 1 mm distance and 512×512 pixels in-plane resolution (see Fig. 3a). Unlike $\mathcal{C}_{nl}$, the CT data for realistic geometries $\mathcal{C}_r$ originated from patient-specific CT scans and had an out-of-plane and in-plane resolution of 0.2 mm.

The generation of an in-silico geometry from such CT data follows a defined workflow. That is, the interface threshold is used to perform a seeded region growing [45] to segment the CT image into air and tissue volumes. Subsequently, the marching cubes algorithm [46] extracts a three-dimensional representation of the air/tissue interface. Stair-step like artifacts from the segmentation are later smoothed away in the mesh generation process. Subsequent developments of a geometry extraction software employ the Medical Interaction Toolkit (MITK) [47], the Insight Toolkit (ITK) [48], and the Visualization Toolkit (VTK) [49]. These libraries enable to generate smooth surfaces by additionally applying a windowed-sinc function smoothing algorithm [50]. Finally, the extraction pipeline ends

with a triangular three-dimensional in-silico model in stereolithography (STL) format which can be used for generating a computational mesh. An example of such a geometry and the corresponding CT data is shown in Fig. 3b.

2.3 Mesh generation

The computational meshes for $\mathcal{G}_{nl}$ were generated using GridPro [51], i.e., block-structured contour-aligned meshes with a maximum number of cells on the order of $\mathcal{O}(10^6)$ were manually created. Depending on the investigation target, the grids were designed to contain 32-34 blocks and possessed a nested O-topology with additional blocks underneath the turbinates (for an example see Fig. 4a). The generation of such meshes is even nowadays difficult and time consuming, especially for such intricate geometries like the nasal cavity. A particular challenge is given by the creation of valid block transitions. As such, the parallel block-nature of such meshes needs to ensure that grid nodes at neighboring block-boundaries coincide, not only to obtain numerical stability but also to avoid the necessity of interpolation. At that time, GridPro could only generate meshes in serial on computers which held way less memory than those of today. Obviously, this introduced an upper bound on the number of possible cells.

Together with an increase of the amount of addressable memory, the mesh type as well as the method for mesh generation changed in the past decade. Hierarchical Cartesian meshes were first used in [24] and [52] for the simulation of the flow in the human nasal cavity and lung. Such meshes have the great advantage that they can be generated fully automatically and that they allow for easy implementations of moving boundary algorithms and local and dynamic mesh refinement. The first version of the new meshing tool [53] was implemented to run in serial. The graph-partitioning library METIS [54] was employed to subdivide the mesh for parallel computation on a fixed number or processes n. Finally, n-many files, each for one process, were written to disk using the NetCDF library [55]. The largest mesh for the simulation of nasal cavity flows that made use of this method consisted of $134.82 \cdot 10^6$ cells and featured a grid distance of $\delta x \approx 0.1\ mm$ [26].

Serial meshing, including domain decomposition and I/O, often required several days, consumed a massive amount of process-local memory, and hence became unsuitable for the realization of high-resolution meshes. Therefore, the meshing process was reinvented in parallel [41]. The newest mesher writes the grid data to disk in parallel by using the high performance computing (HPC) I/O libraries HDF5 [56] or parallel NetCDF [57]. Unlike the serial version, the number of processors to be employed for the computation is not predetermined by the mesher and a quasi arbitrary number of processes can be used for the computation. Furthermore, parallel meshing for high-resolution meshes for large-scale computations can now be generated in a short amount of time on hundreds of thousands of processes without being bound by memory limits, e.g., Lintermann et al. [41] generated $78.54 \cdot 10^9$ cells in 47 s on 262,144 cores of the IBM BlueGene/Q system JUQUEEN at the Jülich Supercomputing Centre (JSC) [58]. The JUQUEEN system consists of 28,672 nodes containing IBM PowerPC A2 CPUs clocked at 1.6 GHz, 16 cores, and 16 GB of RAM. The overall peak performance is 5.9 $PFlops$. The biggest mesh generated so far consists of $640 \cdot 10^9$ cells and its generation took roughly 10 minutes on the whole CRAY XE6 HERMIT system at the High Performance Computing Center Stuttgart (HLRS). Before being replaced by the HORNET HPC system in 2015, HERMIT consisted of 3,552 nodes containing 2 AMD Opteron 6276 (Interlagos) CPUs, each equipped with 16 cores clocked at 2.3 GHz and had a peak performance of 1.045 $PFlops$ for 113,664 cores. 3,072 nodes contained 32 GB of RAM, 480 nodes contained 64 GB of RAM. Parallel I/O was implemented via a

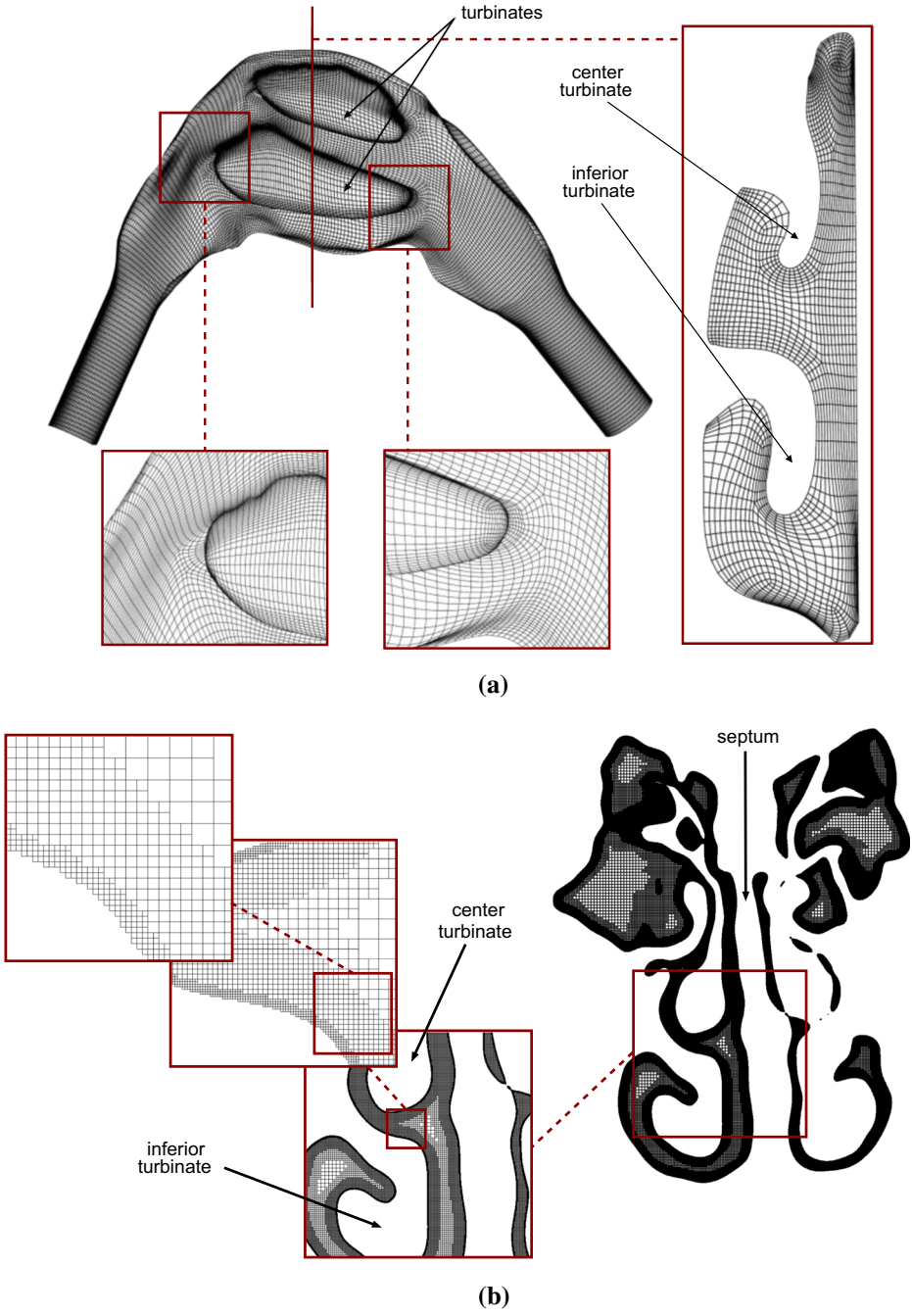

Fig. 4 Structured and unstructured meshes of the nasal cavity for a nose-like geometry $\mathcal{G}_{nl}$ and a geometry $\mathcal{G}_r$ which is based on real patient data. **a** Structured multi-block grid with 450, 000 cells in 34 blocks. The insets show close-ups of the lower turbinate and a cross-section located at the center of the nose-like model. Images taken from [12]. **b** Unstructured grid with $1.8 \cdot 10^9$ cells generated by the parallel grid generator [41]. The insets show consecutive close-ups close to the tissue wall. Every second grid line is shown

Lustre File System (LFS) [59]. In the end, the new mesher also allows for dynamic load-balancing during the meshing. As such, load-imbalance is treated by redistributing cells during the refinement. An example of a hierarchical Cartesian mesh is shown in Fig. 4b.

2.4 Numerical solution of the governing equations

In this section, two different approaches for solving the governing equations of fluid dynamics are briefly introduced. Both methods are employed in Section 3 for an evaluation of the flow in nose-like and realistic nasal cavity geometries. In more detail, Section 2.4.1 discusses a FVM and Section 2.4.2 a LBM. The descriptions are complemented by the corresponding boundary conditions.

2.4.1 Finite volume method

To simulate the flow in $\mathcal{G}_{nl}$, the in-house flow solver TFS of the Institute of Aerodynamics, RWTH Aachen University, has been used. It solves the non-dimensional compressible Navier-Stokes equations with the total density $\tilde{\rho}_0$, the speed of sound based on the stagnation temperature $\tilde{a}_0$, and a characteristic length $\tilde{D}$ as reference values, i.e. the non-dimensional pressure, velocity, and length are obtained by $p = \tilde{p}/(\tilde{\rho}_0\tilde{a}_0^2)$, $u = \tilde{u}/\tilde{a}_0^2$, and $l = \tilde{l}/\tilde{D}$. Temporal integration is performed by a second-order accurate five-stage Runge-Kutta scheme with central-optimized Runge-Kutta coefficients. The inviscid fluxes F_i^I are split into a convective and a pressure term by the advective upstream splitting method (AUSM) [60]. The convective expression is reformulated by inserting the local speed of sound c_s

$$F_i^I = F_i^{c_s} + F_i^p = \frac{U_i}{c_s}\begin{pmatrix}\rho c_s\\ \rho c_s u_j\\ \rho c_s\left(E+\frac{p}{\rho}\right)\end{pmatrix} + \begin{pmatrix}0\\ p\frac{\partial\chi_i}{\partial x_j}\\ 0\end{pmatrix}, \qquad i,j\in\{1,2,3\}, \tag{2}$$

where for a generalized frame of reference $\chi_i(x_j)$ the quantities u_j and U_i represent the Cartesian and the covariant components $U_i = u_j\partial\chi_i/\partial x_j$, with $\partial\chi_i/\partial x_j$ representing the Jacobian transformation matrix. Numerical fluxes $F_i^{c_s}$ on the cell faces in negative and positive directions (denoted by the superscripts "−" and "+") are given by

$$F_i^{c_s} = \frac{1}{2}\left[\frac{Ma_i^+ + Ma_i^-}{2}\left(f_i^{c_s+} + f_i^{c_s-}\right) + \frac{Ma_i^+ + Ma_i^-}{2}\left(f_i^{c_s+} - f_i^{c_s-}\right)\right]. \tag{3}$$

The fluxes $f_i^{\pm}$ and MACH numbers $Ma_i^{\pm}$ are determined by the interpolated variables obtained by a monotonic upstream centered schemes for conservation laws (MUSCL) [61]. For the computation of F_i^p, the expression [62]

$$p^{\pm} = p^{\pm}\left(\frac{1}{2} \pm \frac{Ma_i^{\pm}}{40}\right) \tag{4}$$

is used and for the viscous fluxes a central discretization scheme is chosen.

Boundary conditions A no-slip isothermal condition with $T_{wall} = T_\infty$ and a zero pressure gradient normal to the wall are imposed on the wall. Steady state boundary conditions are based on the equation of Saint-Vernant/Wanzel [63] leading to an iterative scheme at the inlet

$$p_\iota = \left[1 - \frac{\gamma-1}{2}p_{\iota-1}^{-2/\gamma}(\rho_{\iota-1}v_{\iota-1})^2\right]^{\frac{\gamma}{\gamma-1}} \tag{5}$$

for iteration steps $\iota - 1$ and ι and $\gamma = c_p/c_v = 1.4$ is the ratio of specific heats [13]. At the outlet, a static pressure p_∞ is prescribed and a sponge layer prevents reflective behavior. For the simulation of unsteady flow the outlet pressure $p(t)$ is varied temporally to follow a sinusoidal function. At the transition from in- to expiration, the in- and outlet boundary conditions are switched based on the mass flux (see Fig. 5).

2.4.2 *Lattice-Boltzmann method*

The LBM is part of the Zonal Flow Solver (ZFS), developed at the Institute of Aerodynamics and in the HPC section of the Jülich Aachen Research Alliance (JARA-HPC), both RWTH Aachen University. It solves the discretized Boltzmann equation with the simplified right-hand side collision term of the Bhatnagar-Gross-Krook (BGK) approximation [64, 65] for particle probability density distribution functions (PPDFs) f_i for discrete directions i in the D3Q19 [66] model, i.e.,

$$f_i\left(\boldsymbol{x} + \boldsymbol{\xi}_i \delta t, t + \delta t\right) = f_i\left(\boldsymbol{x}, t\right) + \omega \delta t \cdot \left(f_i^{eq}\left(\boldsymbol{x}, t\right) - f_i\left(\boldsymbol{x}, t\right)\right). \tag{6}$$

In this equation the spatial coordinate is given by $\mathbf{x}$, t is the time and δt the time step, $\boldsymbol{\xi}_i$ is the discrete particle speed, the quantity ω represents the collision relaxation factor, and f_i^{eq} is the discrete Maxwellian equilibrium distribution function. The macroscopic variables of the flow are obtained by calculating the moments of the PPDFs. The temperature distribution is simulated by a multi-distribution function (MDF) approach, i.e., by additionally solving

$$g_i\left(\boldsymbol{x} + \boldsymbol{\xi}_i \delta t, t + \delta t\right) = g_i\left(\boldsymbol{x}, t\right) + \Omega \delta t \cdot \left(g_i^{eq}\left(\boldsymbol{x}, t\right) - g_i\left(\boldsymbol{x}, t\right)\right), \tag{7}$$

where Ω is the temperature relaxation parameter. Note that Ω is dependent on the PRANDTL number $Pr = \nu/\kappa$, with κ representing the heat conduction coefficient, while ω is dependent solely on the viscosity ν. Local grid refinement is implemented using the method by Dupuis and Chopard [67] employing different relaxation times per refinement level.

Boundary conditions The no-slip wall-boundary condition uses the interpolated bounce-back formulation by Bouzidi et al. [68] which is second-order accurate. Additionally, body temperature $T_b = 309.15K$ is prescribed by calculating the equilibrium of g_i for a given

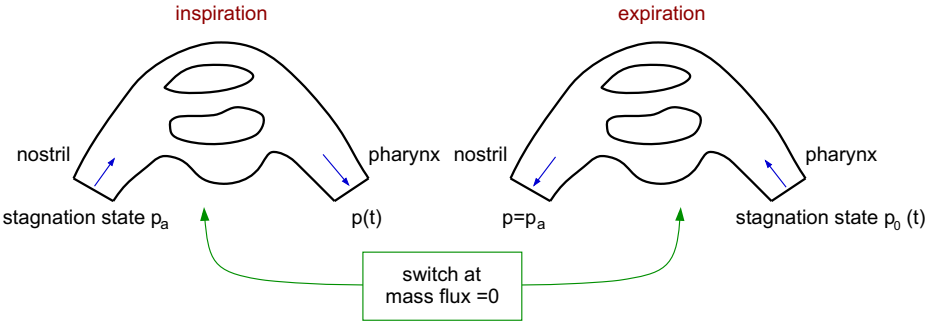

Fig. 5 Handling of unsteady boundary condition in the FVM. At a mass flux of 0 the boundary conditions of the in- and outlet are switched

temperature. Similar to Eq. 5 the inlet uses the reformulated Saint-Vernant/Wanzel equation for the density in LBM-notation [26]

$$\rho_\iota = \left[1 - \frac{\gamma - 1}{2\gamma} \frac{3}{\rho_{\iota-1}^2} (\rho_{\iota-1} v_{\iota-1})^2\right]^{\frac{\gamma}{\gamma-1}} \tag{8}$$

and a temperature $T_\infty = 293.15\ K < T_b$ is prescribed. Instead of setting the pressure at the outlet, a REYNOLDS number-based adaptive density outflow boundary condition is prescribed that relaxes the density ρ_∞ to reach a target REYNOLDS number measured in the outlet plane.

The LBM is well known to have good scalability properties, i.e, simulations can be performed very efficiently [41] and the implementation of boundary conditions is straightforward. Furthermore, as already explained in Section 2.3, the use of hierarchical Cartesian meshes brings great advantages. For these reasons, the transition from the FVM to LBM has been made. Note that all publications from 2010 onward [24–28, 35] employ the LBM for their computations.

3 Results and Discussion

In the following, the experimental and numerical findings using PIV measurements and the FVM (see Sections 2.1 and 2.4.1) are discussed for the flow in a nose-like geometry $\mathcal{G}_{nl}$ (see Figs. 3a and 6). Subsequently, the flow in three realistic patient-based nasal cavity geometries $\mathcal{G}_r = \{\mathcal{N}_g, \mathcal{N}_m, \mathcal{N}_p\}$ is investigated by means of LBM simulations (see Section 2.4.2). As such, this section presents the historical and hierarchical evolution from experimental investigations to those employing low- and high-resolution simulations.

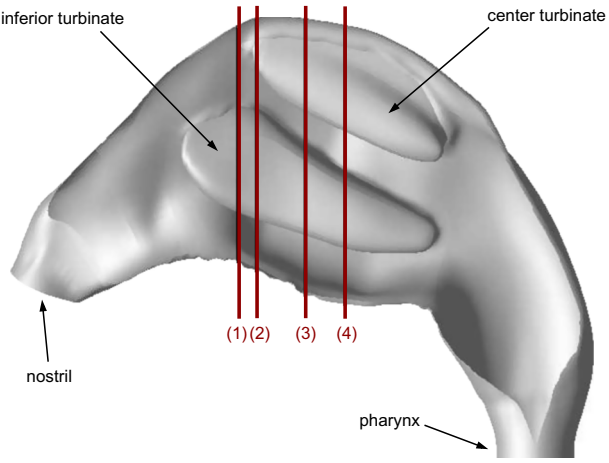

Fig. 6 Geometry $\mathcal{G}_{nl}$ extracted from CT data. The red lines show the locations of cross-sections that are used for the analysis of in-plane velocities in numerical and experimental data

3.1 Experimental and numerical findings for nose-like geometries

The following discussion is based on the results in [12–16], i.e., a thorough comparison of the experimental and numerical findings are presented in Section 3.1.1. Then, the issue of steady vs. unsteady respiration is reflected in Section 3.1.2. Simulations of the flow in the same geometry $\mathcal{G}_{nl}$ are performed, however, two distinct setups $\mathcal{G}_{nl,1}$ and $\mathcal{G}_{nl,2}$ are considered.

The flow solver TFS is used for the simulations and the residuum is reduced by approximately 14 orders of magnitude. The research project had computing time at the HLRS and employed NEC SX-4 and SX-6 machines for the computations.

3.1.1 Comparison of experimental and numerical results

Table 1 summarizes the numerical setup for geometries $\mathcal{G}_{nl,1}$ and $\mathcal{G}_{nl,2}$. The REYNOLDS number $Re = D_h v_b/\nu$ for $\mathcal{G}_{nl,1}$ is defined by the hydraulic diameter $D_h = 4A/C$ at the nostril cross-section, with A denoting the cross-sectional area and C the corresponding circumference, the nostril bulk velocity v_b, and the viscosity of air ν. In contrast, the REYNOLDS number for $\mathcal{G}_{nl,2}$ is based on the hydraulic diameter at the pharynx. Steady state in- and expiratory flow simulations for $\mathcal{G}_{nl,1}$ are based on REYNOLDS numbers of $Re = 1,560$ and $Re = 1,230$, which corresponds to 16.8 l/min and 13.2 l/min. Those for $\mathcal{G}_{nl,2}$ are set to $Re = 500$ and $Re = 400$ defined by the volume fluxes 9.6 l/min and 7.6 l/min. Note that these volume fluxes and REYNOLDS numbers correspond to an in- and expiration through both cavities. The according values in Table 1 are labeled by the subscript $c2$. For simplicity and due to symmetry reasons numerical simulations in $\mathcal{G}_{nl}$ are however only computed in the left cavity. The volume fluxes for these configurations carry the subscript $c1$ in Table 1. The computational meshes for $\mathcal{G}_{nl,1}$ and $\mathcal{G}_{nl,2}$ consist of $450 \cdot 10^3$ and $300 \cdot 10^3$ cells distributed on 34 and 32 parallel blocks.

To validate the numerical analysis, experimental and numerical streamline patterns are juxtaposed for $\mathcal{G}_{nl,1}$ in Fig. 7 at expiration in a cross-section midway between the septum and the upper surface of the turbinates [12]. As such, this velocity distribution is observed

Table 1 Setups for FVM simulations for steady state simulations in $\mathcal{G}_{nl,1}$ and $\mathcal{G}_{nl,2}$ for a single cavity $c1$ and both cavities $c2$ for in- and expiration

Label	Re	D_h	$\dot{V}_{c1}$ $[ml/s]$	$\dot{V}_{c2}$ $[ml/s]$	$\dot{V}_{c2}$ $[l/min]$	Cells	Blocks	State
$\mathcal{G}_{nl,1}$	1,560	n	140.0	280.0	16.8	$450 \cdot 10^3$	34	Inspiration
$\mathcal{G}_{nl,1}$	1,230	n	110.0	220.0	13.2	$450 \cdot 10^3$	34	Expiration
$\mathcal{G}_{nl,2}$	500	p	79.6	159.2	9.6	$300 \cdot 10^3$	32	Inspiration
	1,000	p	159.2	318.3	19.1	$300 \cdot 10^3$	32	
	1,170	p	186.2	372.4	22.4	$300 \cdot 10^3$	32	
	2,500	p	397.9	795.8	47.8	$300 \cdot 10^3$	32	
$\mathcal{G}_{nl,2}$	400	p	63.7	127.3	7.6	$300 \cdot 10^3$	32	Expiration
	790	p	125.7	251.5	15.1	$300 \cdot 10^3$	32	
	1,170	p	186.2	372.4	22.4	$300 \cdot 10^3$	32	
	1,980	p	315.1	630.3	37.8	$300 \cdot 10^3$	32	

The REYNOLDS number Re is based on the reference length D_h found at the nostril n or the pharynx p. Furthermore, the corresponding volume fluxes $\dot{V}$, the mesh size, and the number of blocks for parallel computation are given

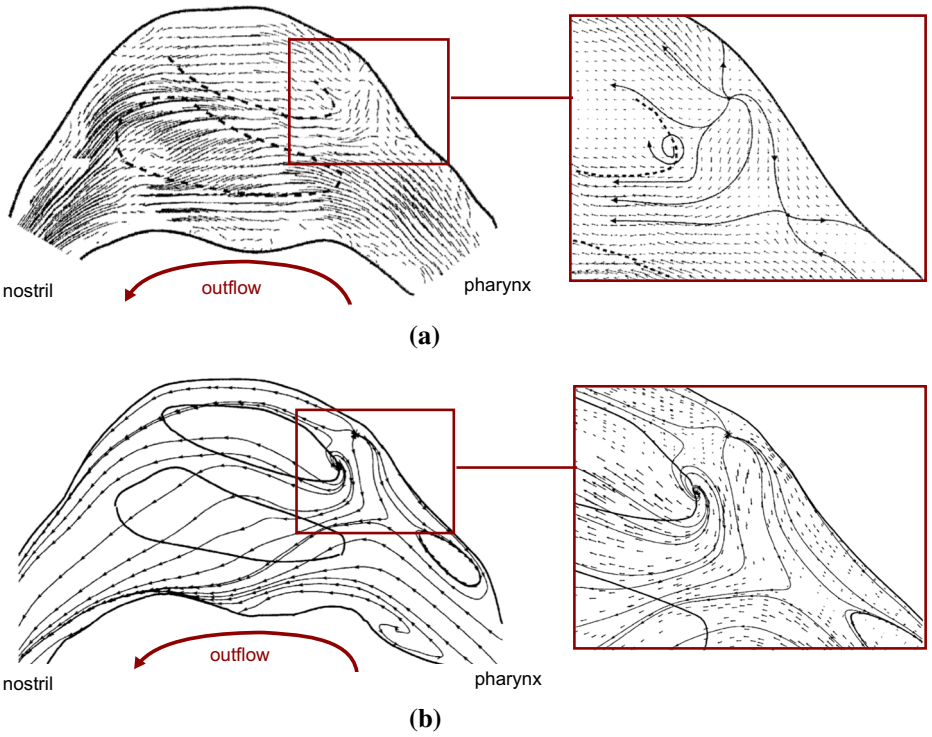

Fig. 7 Comparison of experimental and numerical results by streamline visualizations in a horizontal cross-section of nasal cavity $\mathcal{G}_{nl}$ [12]. **a** Streamlines extracted from experimental PIV data for expiration. **b** Streamlines extracted from numerical data for expiration

in the immediate vicinity of the upper wall for which in Fig. 7 close-ups are shown. The overall flow pattern shows a satisfactory qualitative agreement. The experimental and the numerical findings posses one vortex focus, that is located in the immediate vicinity of the turbinate tip, one source focus and one saddle point next to the upper wall that belong to a reverse flow regime. The experimental and numerical expiratory velocity distribution in four cross-sections of $\mathcal{G}_{nl,2}$ are shown in Fig. 8a and c [13]. The position of these cross-sections are highlighted in Fig. 6. The distributions depicted in cross-sections (3) and (4) emphasize that a strong flow from the region between the upper and lower turbinate through the area between the lower turbinate and the septum exists. Closer to the nostril, in cross-sections (1) and (2), a converging flow structure with a separation line on the septum is determined at almost the same location in the numerical and experimental findings.

The experimental and numerical results for inspiratory flow in $\mathcal{G}_{nl,2}$ are shown in Fig. 8b and d [13]. Obviously, there exists a double vortex structure visible between the lower and upper turbinate in cross-sections (3) and (4). There is a good qualitative agreement between the computations and measurements in the cross-section closest to the pharynx. A slight discrepancy occurs in cross-section (1) since the vortex structure above the lower turbinate is not observed before cross-section (2) in the experiments whereas the numerical analysis reveals such a vortical structure already in cross-section (1). When the less intricate flow region below the lower turbinate is considered, again a satisfactory correspondence between numerics and measurements is visualized.

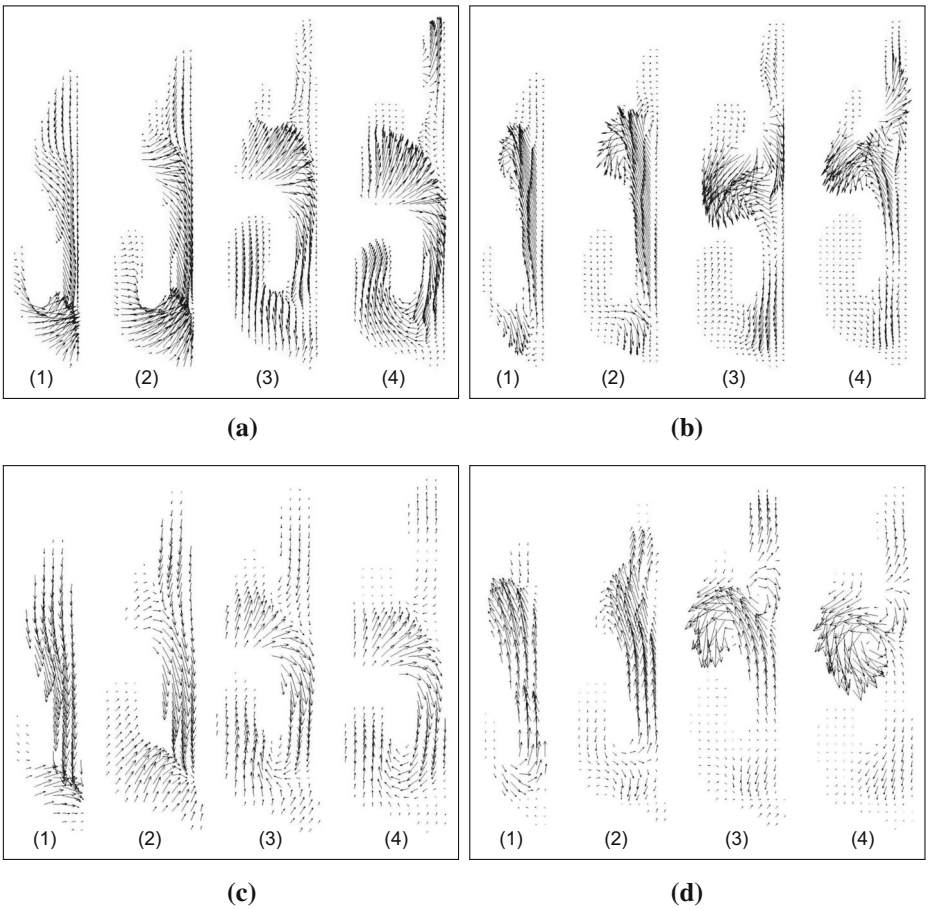

Fig. 8 Numerical and experimental results of nasal cavity flows in geometry $\mathcal{G}_{nl,2}$ for ex- and inspiration at REYNOLDS numbers $Re = 500$ and $Re = 400$. In-plane velocities in individual cross-sections as depicted in Fig. 6 are shown [13]. **a** Num. results: expiration at $Re = 400$. **b** Num. results: inspiration at $Re = 500$. **c** Exp. results: expiration at $Re = 400$. **d** Exp. results: inspiration at $Re = 500$

To summarize, the results in Figs. 7 and 8 show good agreements between computational and experimental results in the saggital and coronal cross-sections. This proves the numerical method and the laminar flow assumption to yield the proper description of the overall flow structure. However, they do not allow to infer any information on unsteady flow under cyclic respiration. Therefore, the results of steady and unsteady simulations are compared next and the major difference between these states is highlighted. For more details on these studies, the reader is referred to [12, 13].

3.1.2 Comparison of steady and unsteady flow

The following findings are based on case $\mathcal{G}_{nl,2}$ for which the REYNOLDS numbers and volume fluxes $\dot{V}$ for the steady state simulations of inspiration and expiration are listed in Table 1 [14, 16]. The unsteady flow simulation covers a REYNOLDS number range of

$0 \leq Re \leq 2900$ for inspiration and $0 \leq Re \leq 2120$ for expiration. The STROUHAL number defined by $Sr = \bar{l}/(t\bar{v})$, where $\bar{l}$ denotes the length of an average nostril-to-pharynx trajectory, t the respiration cycle duration, and $\bar{v}$ the area- and temporal-averaged flow velocity through the nasal cavity for an inspiration, is $Sr = 0.791$. Three respiration cycles were simulated. The first period is skipped because of its dependence on the imposed initial flow condition. The second and third period did not show any difference, which is why the further analysis is based on the second period.

Pressure loss vs. mass flux In Fig. 9a the unsteady pressure loss as a function of mass flux is presented by the thick solid line. The pressure loss is defined by [14, 16]

$$\delta p = \left(p + \frac{\rho}{2}v^2\right)_{nostril} - \left(p + \frac{\rho}{2}v^2\right)_{pharynx} \tag{9}$$

which permits a smooth curve and yields a negative pressure loss at expiration. Figure 9a clearly shows a hysteresis in the pressure loss. The area between the upper and lower curve can be interpreted as additional power loss of the respiration cycle. The expiration phase possesses a higher pressure loss at large mass fluxes than the inspiration phase. The dash-dotted line represents a Bezier fit of the averaged unsteady pressure loss over the mass flux. The shape of this line is in good qualitative agreement with the pressure curves presented in [69]. The results of steady state flows at several REYNOLDS numbers are given by the crosses. It is evident that there is an excellent agreement between the averaged unsteady and the steady state results. This makes sense since the steady state represents a STROUHAL number limit of zero in which case the unsteady thick solid line will approximate the thin solid curve of the Bezier fit. The lower the STROUHAL number the less hysteresis will occur. Also note that when the mass flux decreases in the inspiration and expiration phase the unsteady results are closer to the steady state solution. This observation will be discussed in the following.

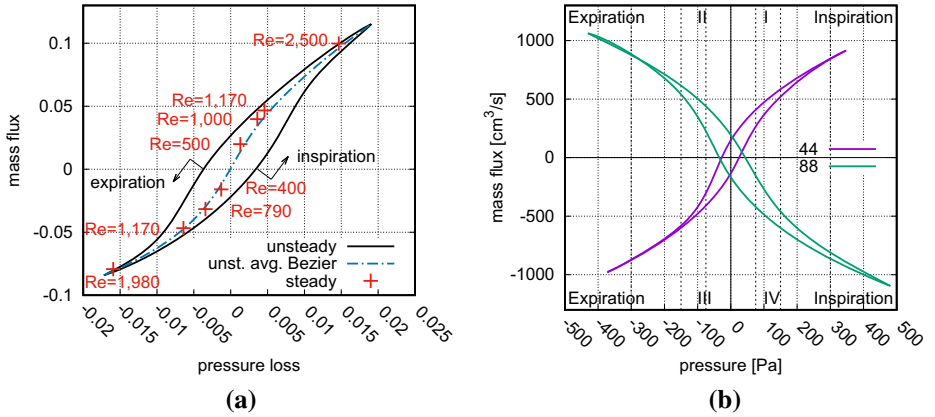

Fig. 9 Juxtaposition of the pressure (loss) vs. the mass flux in numerical simulations in $\mathcal{G}_{nl,2}$ and in 4-phase rhinomanometry measurements in pipe-shaped geometries [14, 16]. **a** Total pressure loss vs. mass flux comparison between steady and unsteady cases in configuration $\mathcal{G}_{nl,2}$. **b** 4-phase rhinomanometry measurements of the static pressure vs. mass flux correlation for the flow in a pipe-shaped nose-model at 44 and 88 $cycles/min$ [70]

Figure 9b shows distributions of the static pressure vs. mass flux based of 4-phase rhinomanometry measurements [70]. A pipe-shaped nose model having a diameter of $d = 6\,mm$ and a length of $l = 100\,mm$ is used at 44 and 88 respiration cycles per minute. The lower respiration frequency is illustrated in quadrant I and III and the higher frequency in quadrant II and IV. The measurements confirm two major results discussed above. First, the shape of the distribution visualizing the fact that at high REYNOLDS numbers or in other words, at high mass fluxes the nasal cavity flow can be assumed steady. Second, the tendency to reduce the hysteresis at lower frequencies. This trend has been described above when the steady state simulations have been discussed.

The further analysis is based on comparisons of $Re = 500$, $Re = 1,170$ at inspiration and $Re = 400$, $Re = 1,170$ at expiration. The results for $Re = 1,000$ and $Re = 790$ are similar to those at $Re = 1,170$ which is why they are skipped in this analysis. At $Re = 2,500$ and $Re = 1,980$ steady and unsteady flow results coincide since there is hardly any hysteresis at such high mass fluxes. Therefore, these results are not addressed in the following discussion. Due to the hysteresis the steady state results are compared with unsteady findings having the equivalent intermediate REYNOLDS number. To enable a direct comparison analogous scales are used for the steady and unsteady results.

Wall-shear stress In the following, the non-dimensional wall-shear stress τ_w, i.e., the skin-friction distributions are compared for steady and unsteady computations [14]. This quantity can be considered to indicate through high values areas endangered of dryness of the mucosa, irritations, and inflammations. The wall-shear stress is computed by the tangential velocity component at the wall-nearest computational cell v_t divided by the wall distance δx_w and multiplied by the dynamic viscosity η, i.e., $\tau_w = \eta \cdot v_t / \delta x_w$. Note that in the following the time labels t_1 and t_2 correspond to increasing and decreasing mass fluxes at unsteady in- or expiration.

All solutions presented in Figs. 10 and 11 possess high wall-shear stress in the region of the nasal valve and the tip of the lower turbinate and lower septum spur. In other words, the flow in the sudden expansion area at the nasal valve does not strongly depend on the temporal changes of the respiration cycle. This is different when the entire surface is considered. At inspiration, an area of high skin friction can be observed on the upper turbinate. The extent of this area undergoes a large variation from covering the complete lower edge at the steady state solution at $Re = 1,170$ and the distribution for the unsteady computation at $Re(t_2) = 1,170$ to the non-existence of this area for the unsteady solution at the increasing mass flux at $Re(t_1) = 500$. Furthermore, there is also high wall-shear stress in the olfactory region for the steady and unsteady solutions at $Re = 1,170$, $Re(t_2) = 1,170$, and $Re(t_2) = 500$. Again, the best match occurs between the steady and unsteady solutions at $Re = 1,170$ and $Re(t_2) = 1,170$, whereas the worst match is obtained for the steady and unsteady solutions, i.e., at $Re = 500$ and $Re(t_1) = 500$. At expiration shown in Fig. 11 the area of high τ_w on the lower edge of the upper turbinate is not observed. It is interesting to note that the overall resemblance of the wall-shear stress distributions between the steady state and unsteady results is definitely better for the expiration than for the inspiration phase. That is, the near-wall flow field seems to be less susceptible to cyclic changes at expiration than inspiration.

In brief, a detailed analysis of the unsteady respiration cycle through a nose-like model of the human nasal cavity was performed at $Sr = 0.791$. The comparison of the steady state and unsteady solutions showed the major differences to occur at increasing mass flux. At decreasing mass flux only small discrepancies between the steady and unsteady findings were observed. Near transition between inspiration and expiration, i.e., at small mass fluxes

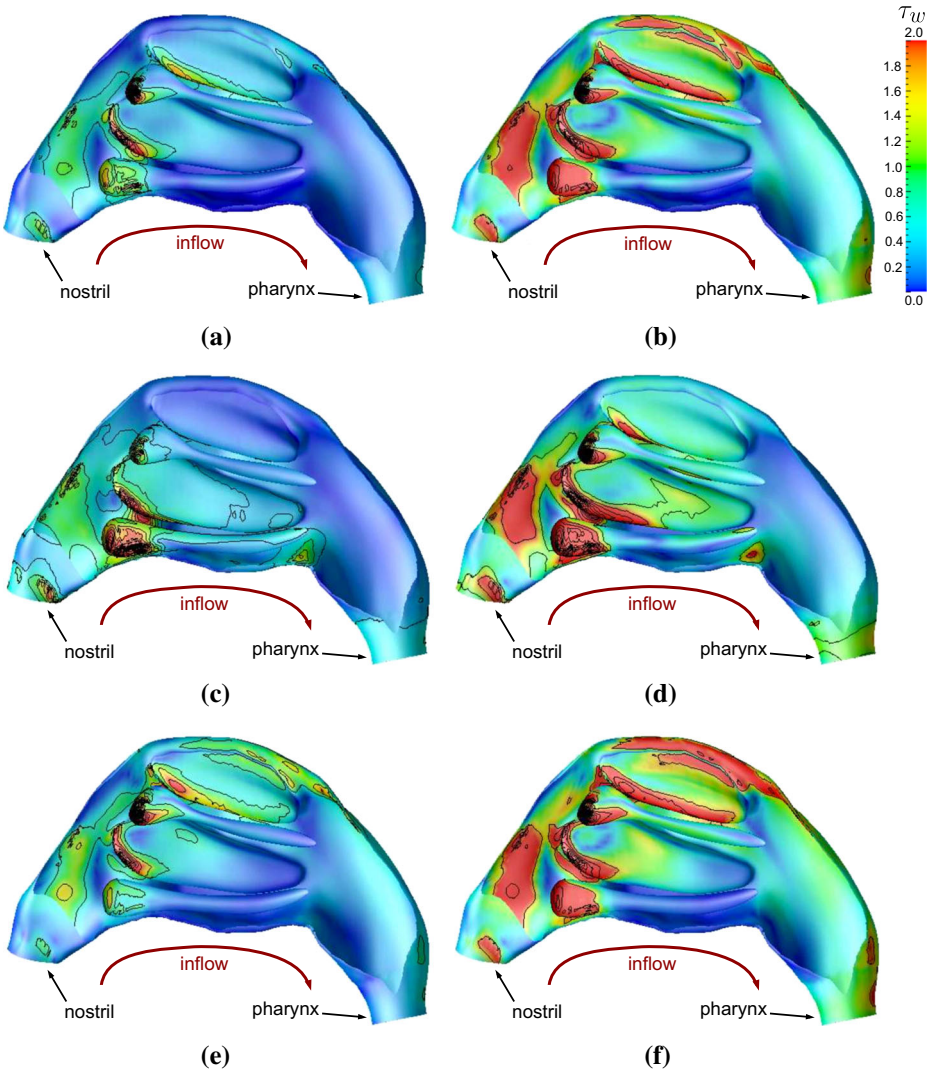

Fig. 10 Comparison of the wall-shear stress τ_w for steady and unsteady inspiration at $Re = \{500; 1170\}$ [14]. **a** Steady inspiration at $Re = 500$. **b** Steady inspiration at $Re = 1,170$. **c** Unst. inspiration at $Re(t_1) = 500$. **d** Unst. inspiration at $Re(t_1) = 1,170$. **e** Unst. inspiration at $Re(t_2) = 500$. **f** Unst. inspiration at $Re(t_2) = 1,170$

the unsteady results are fundamentally different from the steady state solutions. However, at high mass fluxes the characteristic features of the nasal cavity flows are well captured by the steady state solutions. From this analysis, it could be stated as a rule-of-thumb that at $Sr \lesssim 0.8$ it is appropriate to assume the nasal cavity flow to be steady if the REYNOLDS number satisfies $Re > 800$. For more details on the effects of unsteadiness, analyses based on pressure loss along streamlines, streamline distributions, and normalized near-wall velocity vectors at in- and expiration, the reader is referred to [14–16].

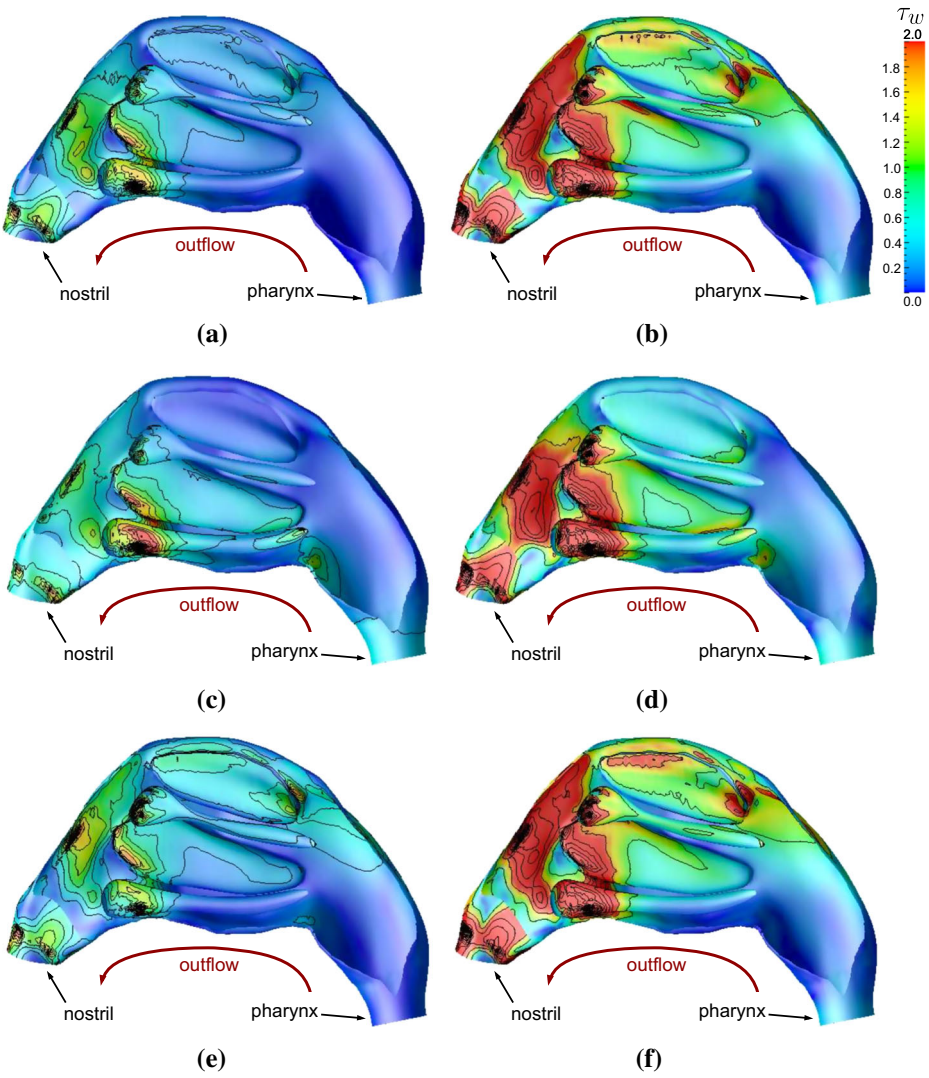

Fig. 11 Comparison of the wall-shear stress τ_w for steady and unsteady expiration at $Re = \{400; 1, 170\}$ [14]. **a** Steady expiration at $Re = 400$. **b** Steady expiration at $Re = 1, 170$. **c** Unst. expiration at $Re(t_1) = 400$. **d** Unst. expiration at $Re(t_1) = 1, 170$. **e** Unst. expiration at $Re(t_2) = 400$. **f** Unst. expiration at $Re(t_2) = 1, 170$

3.2 Classification of anatomically correct nasal cavities

The LBM is used to simulate the steady flow in three anatomically correct nasal cavity geometries $\mathcal{G}_r = \{\mathcal{N}_g, \mathcal{N}_m, \mathcal{N}_p\}$ that have previously been extracted from CT data [26]. The subscripts "g", "m", and "p" represent nasal cavities which were previously classified as good, medium, and poor. This classification is based on a personal evaluation of the patient, who filled out a quality of life questionnaire to determine the rhinosinusitis disability index [71], and on a validation of rhinologists. Nasal cavity $\mathcal{N}_g$ represents a reference case and is considered almost healthy, i.e., it suffers only from a somewhat narrow left nasal cavity

channel. In contrast, $\mathcal{N}_m$ suffers from a septum deviation and from swollen lower and center turbinates inhibiting effective respiration. Configuration $\mathcal{N}_p$ represents a pathological case after surgery, in which on the right side the lower and on the left side the center turbinate have been removed, leaving a large orifice to the left paranasal sinus. Furthermore, the patient suffers from a septum perforation. The surgery aimed at enhancing the respiratory capability of the nasal cavity, however, without taking into account the impact on other physical mechanisms like heating.

The discussion of the results focuses on the pressure loss, vortical structures, the wall-shear stress, and the temperature and heat-flux distribution. The pressure loss can be considered a measure for the mechanical energy loss of inhalation, i.e., to characterize respiratory efficiency. It is a good indicator of comfortable breathing and can be beneficial in pre-surgical analyses. The streamline behavior is analyses to better understand the mixing processes and flux distribution at inspiration. Accelerated flow found at restricted channels may give surgeons a hint on what causes an energy loss and hence, helps to determine loci for surgical interventions. Furthermore, potential areas of irritation and inflammation are detected by the wall-shear stress. Finally, the temperature increase and the heat-flux distribution indicate how efficient the heating capability of the nasal cavity works. This is of special interest, e.g., in cases where large-scale anatomical modifications that decrease the overall surface area of the nasal cavity might lead to a reduced heating capability and hence, to post-surgical discomfort. Table 2 summarizes the simulation setup for the different cases. The REYNOLDS number is based on the hydraulic diameter at the pharynx cross-section D_h, the bulk velocity v_b at $\dot{V} = 250\,ml/s$, and the kinematic viscosity of air ν. Note that all subsequent simulations are based on REYNOLDS numbers $Re > 1,100$ and hence, according to the findings presented in Section 3.1.2, it is sufficient to consider steady flow.

The computations were performed on the Cray XE6 HERMIT of HLRS Stuttgart. Considering the mean velocity in the nasal cavity, it takes approximately $t_c = 5 \cdot 10^5$ iteration steps to cover the distance from the nostrils to the pharynx. Therefore, the initialization and averaging time consist of $t_{c,1} = 4 \cdot t_c$ and $t_{c,2} = 12 \cdot t_c$ iteration steps such that convergence and meaningful statistics are obtained. A grid dependence study shows that a resolution on the finest level of $\delta x = 0.1\,mm$ resulting in meshes consisting of $\mathcal{O}(100^6)$ cells is sufficient. The simulations were run on 2,048 HERMIT cores and took approximately 125 hours. The interested reader is referred to [26] for further details and findings.

3.2.1 Pressure loss

The specific non-dimensional total pressure loss δp (see Eq. 9) between the left and right nasal cavity and the pharynx of the geometries $\mathcal{N}_g$, $\mathcal{N}_m$, and $\mathcal{N}_p$ is considered to evaluate the respiratory efficacy of nasal cavities. In Fig. 12a the values of δp are juxtaposed for

Table 2 Summary of the simulation setup for the three nasal cavities $\mathcal{G}_r = \{\mathcal{N}_g, \mathcal{N}_m, \mathcal{N}_p\}$

Label	Re	D_h	$\dot{V}$ $[ml/s]$	No. cells	Cell res. $[mm]$
$\mathcal{N}_g$	1,597	p	250.0	$134.82 \cdot 10^6$	$101.47 \cdot 10^{-3}$
$\mathcal{N}_m$	1,157	p	250.0	$92.6 \cdot 10^6$	$93.569 \cdot 10^{-3}$
$\mathcal{N}_p$	1,877	p	250.0	$112.76 \cdot 10^6$	$86.626 \cdot 10^{-3}$

The REYNOLDS number Re is based on the reference length D_h found at the pharynx p, the volume flux of 250 ml/s, and the viscosity of air

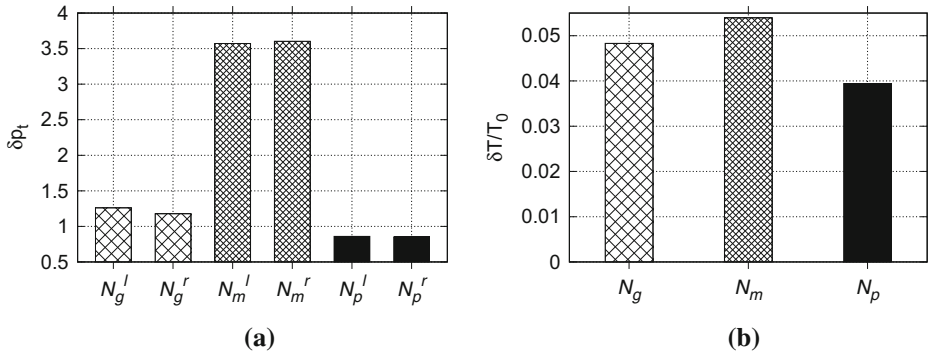

Fig. 12 Non-dimensional total pressure loss and temperature increase in the three nasal cavity configurations $\mathcal{G}_r = \{\mathcal{N}_g, \mathcal{N}_m, \mathcal{N}_p\}$ [26]. **a** Total pressure loss δp. **b** Temperature increase $\delta T / T_\infty$

each side and nasal cavity. It is evident that the lowest pressure loss appears on both sides of nasal cavity $\mathcal{N}_p$ which is due to the surgical removal of large portions of the turbinates in this configuration. The pressure loss of $\mathcal{N}_g$ is slightly increased, especially on the left side which suffers from slightly swollen turbinates. Unlike $\mathcal{N}_p$ and $\mathcal{N}_g$, swollen turbinates and a septum deviation in configuration $\mathcal{N}_m$ lead to a strong increase of the pressure loss and hence to a reduced respiration efficacy and strenuous breathing.

3.2.2 Vortical flow structures

In what follows, the mixing process and corresponding flow structures in the various geometries are analyzed by streamline considerations.

The analysis of the streamlines colored by the velocity magnitude in the side views of configuration $\mathcal{N}_g$ (see Fig. 13a) substantiate the flow in the left cavity to be uniformly distributed. However, the major flux in the right cavity is located in the region of the lower and center turbinate. The low velocity in the left cavity leads to a homogeneous distribution of the flow that is increased in velocity at the end of the turbinates. Unlike the streamwise velocity gradient in $\mathcal{N}_p$ and $\mathcal{N}_m$ the acceleration of the fluid into the pharynx is small.

The illustrations shown in Fig. 13b evidence accelerated flow near the nostrils in the nasal valve of configuration $\mathcal{N}_m$. Downstream of the nasal valves the flow is homogeneously distributed in both nasal cavities. On the left side the flow is split by the lower turbinate, to some extent directed through the small lower channel, and thereby accelerated. Mixing jets dominate the exit region of the turbinate channels and lead to a production of unsteady frequently shed secondary flow structures.

The streamlines in Fig. 13c verify the missing left center turbinate in the nasal cavity $\mathcal{N}_p$ to exceptionally impact the overall flow structure. Like in $\mathcal{N}_m$, the flow is accelerated near the nostril in the nasal valve leading to a jet which is guided toward the back of the nasal cavity. There, it impinges on the tissue and performs a clockwise rotation about the streamwise axis. This way, a recirculation zone is formed. The bulk flow is deflected toward the pharynx, where the left and right cavity merge. The anatomical shape of this region leads to a rotation of the flow about the streamwise axis. The left side and top views show the fluid to enter the left paranasal sinus and to form a slow rotating vortex. Finally, the fluid is accelerated by the converging channel in the pharynx. A septum perforation in the region

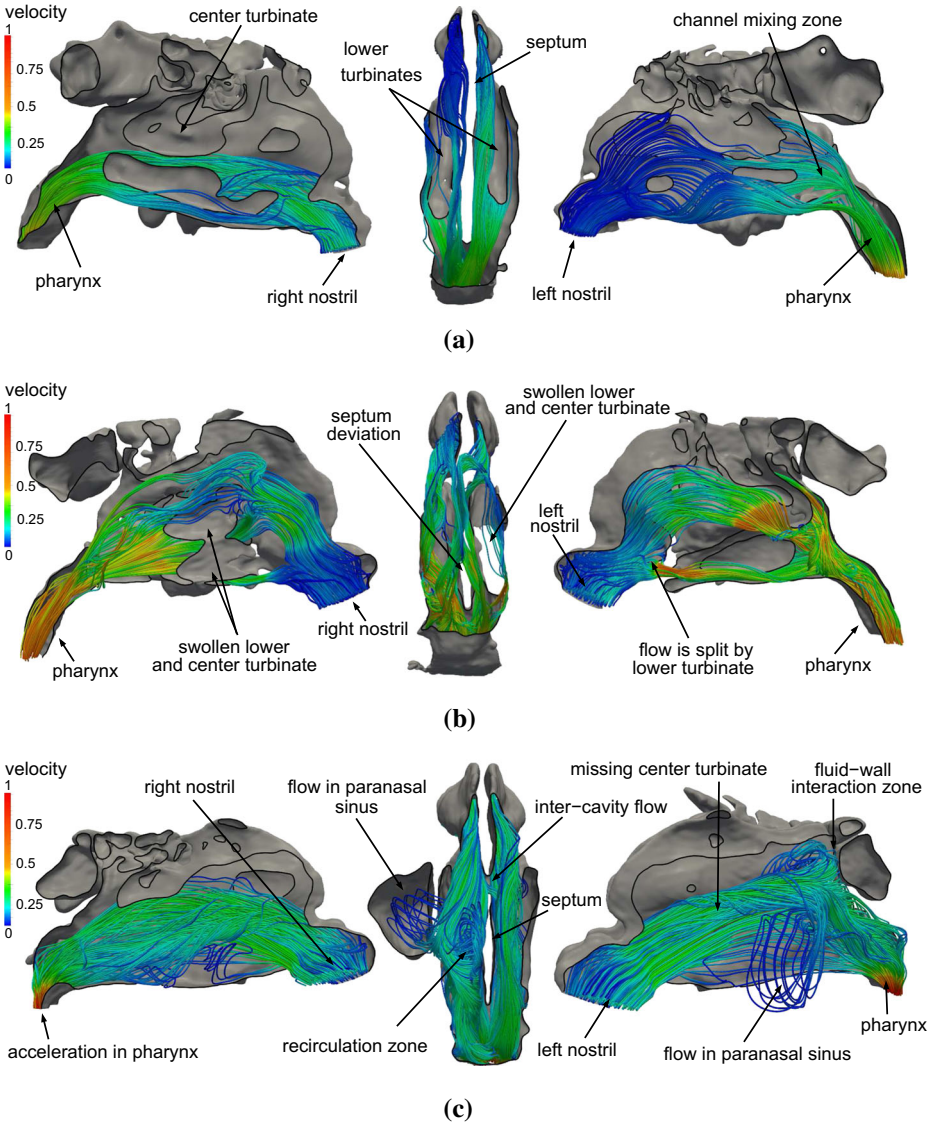

Fig. 13 Streamlines in the the various nasal cavity configurations $\mathcal{G}_r = \{\mathcal{N}_g, \mathcal{N}_m, \mathcal{N}_p\}$. The streamlines are colored by the non-dimensional velocity $v = \bar{v}/\bar{v}_{max}$, where $\bar{v}_{max} = 6.5\ m/s$ [26]. **a** Streamlines in nasal cavity $\mathcal{N}_g$. **b** Streamlines in nasal cavity $\mathcal{N}_m$. **c** Streamlines in nasal cavity $\mathcal{N}_p$

of the missing lower turbinate leads to a mass transfer across the septum and to a slowly tumbling recirculation zone (Fig. 13c).

3.2.3 Wall-shear stress

The non-dimensional wall-shear stress distributions $\tau_w = \bar{\tau}_w / \max\{\bar{\tau}_{w,\{g,m,p\}}\}$ of the configurations $\mathcal{N}_g$, $\mathcal{N}_m$, and $\mathcal{N}_p$ with the overall maximum wall-shear stress value

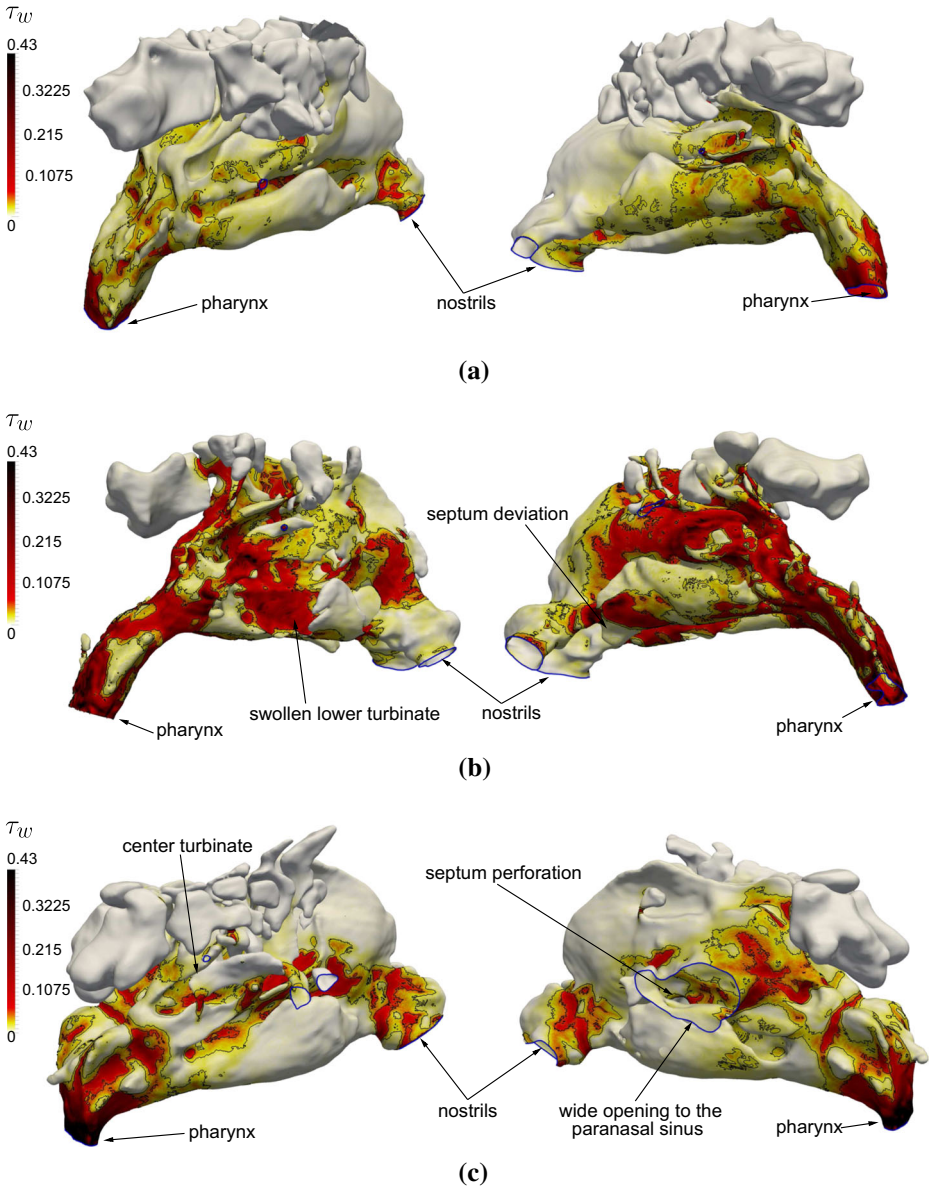

Fig. 14 Wall-shear stress distribution τ_w for the various nasal cavity configurations $\mathcal{G}_r = \{\mathcal{N}_g, \mathcal{N}_m, \mathcal{N}_p\}$. The paranasal sinus have been removed for better visualization [26]. **a** Wall-shear stress τ_w for nasal cavity $\mathcal{N}_g$. **b** Wall-shear stress τ_w for nasal cavity $\mathcal{N}_m$. **c** Wall-shear stress τ_w for nasal cavity $\mathcal{N}_p$

$\max\{\bar{\tau}_{w,\{g,m,p\}}\}$ are shown in Fig. 14. The juxtaposition of the different cases underlines that $\mathcal{N}_g$ has a smoother τ_w distribution than $\mathcal{N}_m$ and $\mathcal{N}_p$, i.e., only some local maxima are observed in regions of converging channels on the left side close to the nostril and in both cavities upstream of the pharynx entrance.

In contrast, configuration $\mathcal{N}_m$ suffers from regions of high wall-shear stress which is due to the overall smaller channel diameters that lead to higher mean flow rates at comparable mass fluxes. In more detail, the smaller cross-section close to the nostrils, i.e., at the nasal valve, leads to a local maximum. Furthermore, a swollen lower turbinate and a strong septum deviation result in high wall-shear stress in the right nasal cavity. On the left side, accelerated by the nasal valve, the fluid impinges on the lower turbinate which causes a locally high τ_w distribution. At the pharynx, where the flow from both sides merges into a mixing zone, a region of high wall-shear stress is produced. The overall maximum is reached at the back of the pharynx, where the fluid is guided downstream to the larynx.

Similar to $\mathcal{N}_g$ and $\mathcal{N}_m$, the flow in configuration $\mathcal{N}_p$ is accelerated in the nasal valves which leads to local wall-shear stress maxima. On the left side, downstream of the large orifice to the paranasal sinus (see Fig. 14c), the interaction of the fluid with the outer back wall causes increased τ_w. The center turbinate has surgically been removed and a wide opening to the paranasal sinus exists on this side. As such, the jet emerging from the nasal valve is directly guided against the nasal cavity wall which causes the increased τ_w distribution. The septum perforation leads to a mass flow from the left to the right nasal cavity and experiences an elevated τ_w. On the right side, the converging channel in the region of the center turbinate is dominated by increased wall-shear stress. Further downstream, a ring of high τ_w is formed due to the converging-diverging channel geometry. However, the highest wall-shear stress is again determined further downstream in the pharynx due to the accelerated flow.

3.2.4 Heating capability

To complement the evaluation of the respiration efficiency of the nasal cavities the temperature increase of the flow, which is a function of the residence time of the fluid in the nasal cavity, is discussed next. That is, the heating capability is determined by considering the temperature increase $\delta T/T_\infty$ from the nostril to the pharynx. Ideally, the flow through the nasal cavity is heated up to almost body temperature $T_b = 309.15\ K$ or in other words the non-dimensional $\delta\tilde{T}$ takes a value of $\delta\tilde{T}_b = 0.0546$. Considering the heating capability shown in Fig. 12b for the configurations $\mathcal{N}_g$, $\mathcal{N}_m$, and $\mathcal{N}_p$, the nasal cavity $\mathcal{N}_m$ has the most efficient heating capability and increases the temperature almost up to T_b. The heating capability of $\mathcal{N}_g$ is slightly smaller than that of $\mathcal{N}_m$, and clearly higher than that of $\mathcal{N}_p$. The lower temperature increase for $\mathcal{N}_p$ is due to the reduced surface area and the less intricate geometry of the cavity, which prevents a pronounced mixing and as such reduces the residence time of the fluid in the cavity.

Figure 15 shows the non-dimensional heat flux distribution $\dot{q} = \kappa \cdot \partial T/\partial n|_{x=0}$ at the iso-thermal wall at distance $x = 0$, where κ is the thermal conductivity and n is the wall normal. The temperature profile along this normal is represented by a second-order polynomial. The temperature values are trilinearly interpolated and separated by δx. Note that $\dot{q}$ is normalized by the overall maximum $\max\{\dot{q}_r\}$ of the configurations $\mathcal{G}_r$. The heat flux range in Fig. 15 was chosen to visualize differences between locally high $\dot{q}$ values. For reference, Table 3 shows the dynamic range in absolute values and in percent related to $\max\{\dot{q}_r\}$. As evidenced in Fig. 15a the distributions of the the heat flux for configuration $\mathcal{N}_g$ is best as it smoothly increases from the nostrils to the pharynx. Especially in the right nasal cavity, which features a low pressure loss as well as subsided turbinates, $\dot{q}$ continuously increases along the streamwise direction. Unlike on the right side, $\dot{q}$ is almost equally distributed between the turbinate channels on the left side. The major heat flux occurs in the retral part

Table 3 Minimum and maximum values of the normalized heat flux $\dot{q}$ for the different configurations

Label	$\min\{\dot{q}_{\mathcal{N}_r}\}$	$\max\{\dot{q}_{\mathcal{N}_r}\}$	$\delta\dot{q}$ [%]
$\mathcal{N}_g$	0.6052	1.0	39.48
$\mathcal{N}_m$	0.9377	0.9998	6.21
$\mathcal{N}_p$	0.9358	0.9992	6.34

Additionally, the according dynamic range $\delta\dot{q}$ is given in percent related to $\max\{\dot{q}_r\}$

of the turbinate channels and the pharynx. As shown in Fig. 15b the heat flux distribution in configuration $\mathcal{N}_m$ is dominated by local maxima in the retral part of the turbinate channels while in the lower turbinate channel of the left nasal cavity in the channel mixing zone of the right cavity, and in the pharynx region a smooth distribution is determined. In contrast to configuration $\mathcal{N}_g$ the overall $\dot{q}$ distribution is however decreased. The low heat flux distribution of configuration $\mathcal{N}_p$ in Fig. 15c emphasizes the low heating capability of this nasal cavity.

To summarize, the investigations revealed a removal of turbinates to lead to a lower total drag such that less energy is necessary to inhale. However, the heating capability is lower compared to the other configurations due to the reduced surface area. The local wall-shear stress is highest in the poor configuration resulting in an increased potential inflammation load. The septum deviation and the swollen turbinates in the medium configuration lead to the highest averaged wall-shear stress. The heating capability is best for the medium geometry although the surface area and the overall heat flux distribution is smaller than that of the good configuration. However, the heating capability is strongly dependent on the flow distribution and does not necessarily correlate with the surface area and the heat flux distribution. The good configuration possesses a slightly lower heating capability and the averaged wall-shear stress distribution is lowest. These results are in good agreement with the results from the rhinosinusitis disability index questionnaire filled out by the patients and the evaluation by radiologists.

A comparison of the results to those obtained in Section 3.1 shows that the flow fields are fundamentally different in model and anatomically correct nasal cavities. Obviously, realistic airways obtained from CT data can become arbitrarily complex preventing a meaningful comparison to the model case. A juxtaposition to experiments as presented for model geometries is difficult since the flow parameter cannot be easily accessed in-vivo without altering the flow. Furthermore, the physics, that determines the respiratory capability, heating capability, and the sensitivity to the formation of inflammatory regions, is highly subject- and pathology-dependent. This leads to the necessity to evaluate each clinical case individually.

4 Summary and Outlook

The fluid mechanics of nose-like and real nasal cavities has been experimentally and numerically analyzed by digital particle image velocimetry, a finite volume, and a lattice-Boltzmann method. It has been the flow physics not the numerical and experimental methods that has defined the core of the discussion.

First, the steady flow through a nose-like model has been analyzed and juxtaposed to experimental findings for in- and expiration. The comparison has shown the numerical

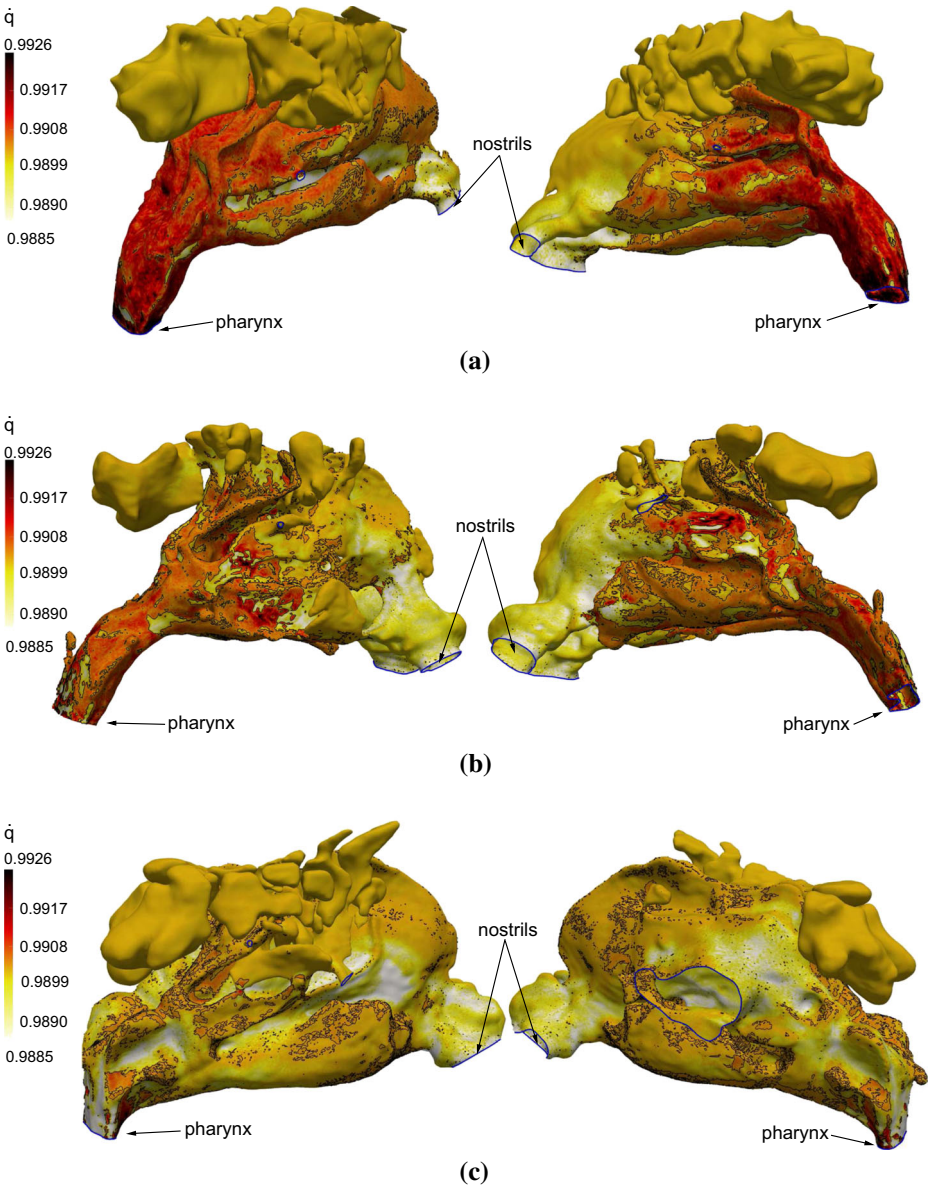

Fig. 15 Heat flux distribution $\dot{q}$ for the various nasal cavity configurations $\mathcal{G}_r = \{\mathcal{N}_g, \mathcal{N}_m, \mathcal{N}_p\}$. The paranasal sinus have been removed for better visualization [26]. **a** Heat flux $\dot{q}$ for nasal cavity $\mathcal{N}_g$. **b** Heat flux $\dot{q}$ for nasal cavity $\mathcal{N}_m$. **c** Heat flux $\dot{q}$ for nasal cavity $\mathcal{N}_p$

results to be in good agreement with the experimental findings. Subsequently, the unsteady flow for the complete respiration cycle has been analyzed and compared to steady state solutions for inspiration and expiration. As a rule-of-thumb the flow in the nasal cavity can be assumed steady for STROUHAL numbers $Sr \lesssim 0.8$ and REYNOLDS numbers $Re > 800$. Based on these results, the analysis of three anatomically correct in-silico nasal cavity

geometries has been performed for steady inspiratory flow at rest. The results have been used to classify the nasal cavities from a fluid mechanics point of view. The classification is based on the evaluation of the pressure loss, streamline considerations, wall-shear stress distribution, heating capability, and heat flux distribution at the tissue surface. The results are in good agreement with subjective evaluations of the patients and with the according diagnoses of medical experts. They deliver detailed insight into the fundamental flow physics of respiration for individual patients and can be beneficial in pre-surgical procedural planning.

The presented approaches have underlined that the algorithms have grown mature and are ready for an integration into clinical tests. They allow highly detailed computations of steady and unsteady in- and expiratory flows. In this regard, the lattice-Boltzmann method has shown to be a cost-efficient approach for such computations. In light of the increasing power of today's computer systems it is just a matter of years until such methods will be considered for clinical applications.

A major challenge will be given by increasing both the user-friendliness of such approaches and their acceptance among medical doctors. As such, the transition from a research code to a user-friendly software whose execution for an individual pathological case can be commissioned by surgeons as well as the automatic extraction of surgery-relevant data and suggestions still needs to be tackled. Such a tool in conjunction with large-scale databases of pathological cases will furthermore enable to extract surgery suggestions for new pathological cases from known cases via datamining and artificial intelligence algorithms. Also, the integration of shape-optimization algorithms will allow to optimize the anatomical structure with respect to increased respiratory efficiency by minimizing the pressure loss and wall-shear stress and by maximizing the heating and moisturization capability.

There is still room for improvement from a modeling perspective. To improve the similarity between realistic and simulated respiration, effects of nasal hair, wall-bounded fluid transport, and tissue movement could be considered to be included. Examples where fluid-structure interactions play a role are the nasal valve effect, which causes a narrowing of the airway at inspiration, the movement of the suppository and the soft palate when snoring, or even the airway collapse in obstructive sleep apnea syndrome patients. Inclusion of these aspects on the one hand will increase the computational effort and on the other hand, will enhance the solutions of the simulations. The model development and numerical implementations are still an active field of research.

Acknowledgements The authors of this manuscript would like to thank Dr.-Ing. Ingolf Hörschler and Dr.-Ing. Matthias Meinke for the provision of visual material and fruitful discussions. The research for this project has been conducted under DFG research grant WE-2186/5. Furthermore, the authors gratefully acknowledge the computing time granted by the JARA-HPC Vergabegremium and provided on the JARA-HPC Partition, part of the supercomputer JUQUEEN [58] at Forschungszentrum Jülich and the Gauss Centre for Supercomputing (GCS) for providing computing time through the John von Neumann Institute for Computing (NIC) on the GCS share of JUQUEEN and the HERMIT at HLRS Stuttgart. GCS is the alliance of the three national supercomputing centers HLRS (Universität Stuttgart), JSC (Forschungszentrum Jülich), and LRZ (Bayerische Akademie der Wissenschaften), funded by the German Federal Ministry of Education and Research (BMBF) and the German State Ministries for Research of Baden-Württemberg (MWK), Bayern (StMWFK) and Nordrhein-Westfalen (MIWF).

Compliance with Ethical Standards This study was funded by the German Research Foundation (DFG) under research grant number WE-2186/5.

Conflict of interests The authors declare that they have no conflict of interest.

References

1. Maune, S., Rudert, H., Heissenberg, M., Schmidt, C., Eggers, S., Landmann, K., Küchler, T.: Concepts for measuring quality of life in patients with chronic sinusitis. Laryngorhinootologie **78**(9), 475 (1999). https://doi.org/10.1055/s-2007-996912
2. Damm, M., Quante, G., Jungehuelsing, M., Stennert, E.: Impact of functional endoscopic sinus surgery on symptoms and quality of life in chronic rhinosinusitis. Laryngoscope **112**(2), 310 (2002). https://doi.org/10.1097/00005537-200202000-00020
3. Croy, I., Hummel, T., Pade, A., Pade, J.: Quality of life following nasal surgery. Laryngoscope **120**(4), 826 (2010). https://doi.org/10.1002/lary.20824
4. Stammberger, H., Posawetz, W.: Functional endoscopic sinus surgery. Concept, indications and results of the Messerklinger technique. Eur. Arch. Otorhinolaryngol. **247**(2), 63 (1990)
5. Giles, W.C., Gross, C.W., Abram, A.C., Greene, W.M., Avner, T.G.: Endoscopie septoplasty. Laryngoscope **104**(12), 1507 (1994). https://doi.org/10.1288/00005537-199412000-00015
6. Hol, M.K., Huizing, E.H.: Treatment of inferior turbinate pathology: a review and critical evaluation of the different techniques. Rhinology **38**(4), 157 (2000)
7. Senior, B.A., Kennedy, D.W., Tanabodee, J., Kroger, H., Hassab, M., Lanza, D.: Long-term results of functional endoscopic sinus surgery. Laryngoscope **108**(2), 151 (1998)
8. Chhabra, N., Houser, S.M.: The diagnosis and management of empty nose syndrome. Otolaryngol. Clin. North Am. **42**(2), 311 (2009). https://doi.org/10.1016/j.otc.2009.02.001
9. Batra, P.S., Seiden, A.M., Smith, T.L.: Surgical management of adult inferior turbinate hypertrophy. Laryngoscope **119**(9), 1819 (2009). https://doi.org/10.1002/lary.20544
10. Bhandarkar, N.D., Smith, T.L.: Outcomes of surgery for inferior turbinate hypertrophy. Curr. Opin. Otolaryngol. Head Neck Surg. **18**(1), 49 (2010). https://doi.org/10.1097/MOO.0b013e328334d974
11. Adams, L., Krybus, W., Meyer-Ebrecht, D., Rueger, R., Gilsbach, J., Moesges, R., Schloendorff, G.: Computer-assisted surgery. IEEE Comput. Graph. Appl. **10**(3), 43 (1990). https://doi.org/10.1109/38.55152
12. Hörschler, I., Meinke, M., Schröder, W.: Numerical simulation of the flow field in a model of the nasal cavity. Comput. Fluids **32**(1), 39 (2003). https://doi.org/10.1016/S0045-7930(01)00097-4
13. Hörschler, I., Brücker, C., Schröder, W., Meinke, M.: Investigation of the impact of the geometry on the nose flow. Eur. J. Mech. B. Fluids **25**(4), 471 (2006). https://doi.org/10.1016/j.euromechflu.2005.11.006
14. Hörschler, I., Schröder, W., Meinke, M.: Comparison of steady and unsteady nasal cavity flow solutions for the complete respiration cycle. Comput. Fluid Dyn. J. **15**(3), 354 (2006)
15. Hörschler, I., Schröder, W.: On the geometry dependence of the nose flow. In: van Steenhoven, A. (ed.) Ercoftac Bulletin, vol. 68 (2006)
16. Hörschler, I., Schröder, W., Meinke, M.: On the assumption of steadiness of nasal cavity flow. J. Biomech. **43**(6), 1081 (2010). https://doi.org/10.1016/j.jbiomech.2009.12.008
17. Naftali, S., Schroter, R.C., Shiner, R.J., Elad, D.: Transport phenomena in the human nasal cavity: a computational model. Ann. Biomed. Eng. **26**(5), 831 (1998)
18. Naftali, S., Rosenfeld, M., Wolf, M., Elad, D.: The air-conditioning capacity of the human nose. Ann. Biomed. Eng. **33**(4), 545 (2005). https://doi.org/10.1007/s10439-005-2513-4
19. Finck, M., Hänel, D., Wlokas, I.: Simulation of nasal flow by lattice Boltzmann methods. Comput. Biol. Med. **37**(6), 739 (2007). https://doi.org/10.1016/j.compbiomed.2006.06.013
20. Elad, D., Naftali, S., Rosenfeld, M., Wolf, M.: Physical stresses at the air-wall interface of the human nasal cavity during breathing. J. Appl. Physiol. **100**(3), 1003 (2006). http://doi.org/10.1152/japplphysiol.01049.2005
21. Zachow, S., Steinmann, A., Hildebrandt, Th., Weber, R., Heppt, W.: CFD simulation of nasal airflow: Towards treatment planning for functional rhinosurgery. Int. J. Comput. Assist. Radiol. Surg. **1**(S1), 147–167 (2006). https://doi.org/10.1007/s11548-006-0018-8
22. Yu, S., Liu, Y., Sun, X., Li, S.: Exploiting lustre file joining for effective collective IO. Rhinology **46**(2), 137 (2008)
23. Riazuddin, V.N., Zubair, M., Shuaib, I.L., Abdullah, M.Z., Hamid, S.A., Ahmad, K.A.: Numerical study of inspiratory and expiratory flow in a human nasal cavity. J. Med. Biol. Eng. **31**(3), 201 (2010). https://doi.org/10.5405/jmbe.781
24. Eitel, G., Freitas, R.K., Lintermann, A., Meinke, M., Schröder, W.: Numerical simulation of nasal cavity flow based on a Lattice-Boltzmann method. In: Dillmann, A., Heller, G., Klaas, M., Kreplin, H.-P., Nitsche, W., Schröder, W. (eds.) New Results in Numerical and Experimental Fluid Mechanics VII,

Notes on Numerical Fluid Mechanics and Multidisciplinary Design, vol. 112, pp. 513–520. Springer, Berlin (2010)
25. Lintermann, A., Eitel-Amor, G., Meinke, M., Schröder, W.: Lattice-Boltzmann solutions with local grid refinement for nasal cavity flows. In: New Results in Numerical and Experimental Fluid Mechanics VIII, pp. 583–590. Springer (2013). https://doi.org/10.1007/978-3-642-35680-3_69
26. Lintermann, A., Meinke, M., Schröder, W.: Fluid mechanics based classification of the respiratory efficiency of several nasal cavities. Comput. Biol. Med. **43**(11), 1833 (2013). https://doi.org/10.1016/j.compbiomed.2013.09.003
27. Lintermann, A., Meinke, M., Schröder, W.: Investigations of nasal cavity flows based on a Lattice-Boltzmann method. In: Resch, M., Wang, X., Bez, W., Focht, E., Kobayashi, H., Roller, S. (eds.) High Performance Computing on Vector Systems 2011, pp. 143–158. Springer, Berlin (2012). https://doi.org/10.1007/978-3-642-22244-3
28. Lintermann, A., Meinke, M., Schröder, W.: Investigations of the inspiration and heating capability of the human nasal cavity based on a Lattice-Boltzmann method. In: Proceedings of the ECCOMAS Thematic International Conference on Simulation and Modeling of Biological Flows (SIMBIO 2011), vol. 2011, Brussels (2011)
29. Gambaruto, A., Taylor, D., Doorly, D.: Modelling nasal airflow using a Fourier descriptor representation of geometry. Int. J. Numer. Methods Fluids **59**(11), 1259 (2009). https://doi.org/10.1002/fld.1866
30. Gambaruto, A.M., Taylor, D.J., Doorly, D.J.: Decomposition and description of the nasal cavity form. Ann. Biomed. Eng. **40**(5), 1142 (2012). https://doi.org/10.1007/s10439-011-0485-0
31. Calmet, H., Gambaruto, A.M., Bates, A.J., Vázquez, M., Houzeaux, G., Doorly, D.J.: Large-scale CFD simulations of the transitional and turbulent regime for the large human airways during rapid inhalation. Comput. Biol. Med. **69**, 166 (2016). https://doi.org/10.1016/j.compbiomed.2015.12.003
32. Henn, T., Thäter, G., Dörfler, W., Nirschl, H., Krause, M.J.: Parallel dilute particulate flow simulations in the human nasal cavity. Comput. Fluids **124**, 197 (2016). https://doi.org/10.1016/j.compfluid.2015.08.002
33. Shang, Y., Inthavong, K., Tu, J.: Detailed micro-particle deposition patterns in the human nasal cavity influenced by the breathing zone. Comput. Fluids **114**, 141 (2015). https://doi.org/10.1016/j.compfluid.2015.02.020
34. Bates, A.J., Doorly, D.J., Cetto, R., Calmet, H., Gambaruto, A.M., Tolley, N.S., Houzeaux, G., Schroter, R.C.: Dynamics of airflow in a short inhalation. J. R. Soc. Interface **12**(102), 20140880 (2014). https://doi.org/10.1098/rsif.2014.0880
35. Lintermann, A.: Efficient parallel geometry distribution for the simulation of complex flows. In: Papadrakakis, M., Papadopoulos, V., Stefanou, G., Plevris, V. (eds.) VII European Congress on Computational Methods in Applied Sciences and Engineering, Hersonissos (2016)
36. Engelhardt, L., Röhm, M., Mavoungou, C., Schindowski, K., Schafmeister, A., Simon, U.: First steps to develop and validate a CFPD model in order to support the design of nose-to-brain delivered biopharmaceuticals. Pharm. Res. (2016). https://doi.org/10.1007/s11095-016-1875-7
37. Wilcox, D.C.: Turbulence Modeling for CFD, 3rd edn. DCW Industries, Inc. ISBN 978-1928729082 (2006)
38. Grotjans, H., Menter, F.: Wall functions for industrial applications. In: Papailiou, K.D. (ed.) Computational fluid dynamics '98, ECCOMAS, pp. 1112–1117. Wiley, New York (1998)
39. Chien, K.Y.: Predictions of channel and boundary-layer flows with a low-Reynolds-number turbulence model. AIAA J. **20**(1), 33 (1982). https://doi.org/10.2514/3.51043
40. Smagorinsky, J.: General circulation experiments with the primitive equations. Mon. Weather Rev. **91**(3), 99 (1963). https://doi.org/10.1175/1520-0493(1963)091<0099:GCEWTP>2.3.CO;2
41. Lintermann, A., Schlimpert, S., Grimmen, J., Günther, C., Meinke, M., Schröder, W.: Massively parallel grid generation on HPC systems. Comput. Methods Appl. Mech. Eng. **277**, 131 (2014). https://doi.org/10.1016/j.cma.2014.04.009
42. Raffel, M., Willert, C., Wereley, S., Kompenhans, J.: Particle image velocimetry, 2nd edn. In: Experimental Fluid Mechanics. Springer, Berlin (2007). https://doi.org/10.1007/978-3-540-72308-0
43. Brücker, C., Park, K.I.: Experimental study of velocity fields in a model of human nasal cavity by DPIV. In: Banerjee, S., Eaton, K. (eds.) First International Symposium on Turbulence and Shear Flow Phenomena, Santa Barbara, pp. 831–842 (1999)
44. Masing, H.: Experimentelle Untersuchungen über die Strömung im Nasenmodell. Eur. Arch. Otorhinolaryngol. **189**(1), 59 (1967)
45. Adams, R., Bischof, L.: Seeded region growing. IEEE Trans. Pattern Anal. Mach. Intell. **10**(3), 43–51 (1990). https://doi.org/10.1109/34.295913

46. Lorensen, W.E., Cline, H.E.: Marching cubes: a high resolution 3D surface construction algorithm. ACM SIGGRAPH Computer Graphics **21**(4), 163 (1987)
47. Nolden, M., Zelzer, S., Seitel, A., Wald, D., Müller, M., Franz, A.M., Maleike, D., Fangerau, M., Baumhauer, M., Maier-Hein, L., Maier-Hein, K.H., Meinzer, H.P., Wolf, I.: The medical imaging interaction toolkit: challenges and advances : 10 years of open-source development. Int. J. Comput. Assist. Radiol. Surg. **8**(4), 607 (2013). https://doi.org/10.1007/s11548-013-0840-8
48. Ibanez, L., Schroeder, W., Ng, L., Cates, J.: The ITK Software Guide, 1st edn. Kitware, Inc., ISBN 1-930934-10-6 (2003)
49. Schroeder, W., Ken, M., Lorensen, B.: The Visualization Toolkit, 4th edn. Kitware, Inc., ISBN 978-1-930934-19-1 (2006)
50. Taubin, G., Zhang, T., Golub, G.: Optimal surface smoothing as filter design. Computer Vision—ECCV'96 **20404**, 283 (1996)
51. GridPro, The CFD Link to Design, The Graphic Manager Manual. Programm Development Corp. 300 Hamilton Ave. Suite 409, White Plains, N.Y. 10601, USA
52. Freitas, R.K., Schröder, W.: Numerical investigation of the three-dimensional flow in a human lung model. J. Biomech. **41**(11), 2446 (2008). https://doi.org/10.1016/j.jbiomech.2008.05.016
53. Hartmann, D., Meinke, M., Schröder, W.: An adaptive multilevel multigrid formulation for Cartesian hierarchical grid methods. Comput. Fluids **37**(9), 1103 (2008). https://doi.org/10.1016/j.compfluid.2007.06.007
54. Karypis, G., Kumar, V.: A parallel algorithm for multilevel graph partitioning and sparse matrix ordering. J. Parallel Distrib. Comput. **48**(1), 71 (1998). https://doi.org/10.1006/jpdc.1997.1403
55. UCAR/Unidata, NetCDF library 3.x, Boulder. (2003). https://doi.org/10.5065/D6RN35XM
56. Folk, M., Pourmal, E.: Balancing performance and preservation lessons learned with HDF5. In: Proceedings of the 2010 Roadmap for Digital Preservation Interoperability Framework Workshop on - US-DPIF '10, pp. 1–8 (2010). https://doi.org/10.1145/2039274.2039285
57. Li, J., Zingale, M., Liao, W.k., Choudhary, A., Ross, R., Thakur, R., Gropp, W., Latham, R., Siegel, A., Gallagher, B.: Parallel netCDF: a high-performance scientific I/O interface. In: Proceedings of the 2003 ACM/IEEE conference on Supercomputing - SC '03, p. 39. ACM Press, New York (2003). https://doi.org/10.1145/1048935.1050189
58. Stephan, M., Docter, J.: JUQUEEN: IBM blue gene/Q® supercomputer system at the Jülich supercomputing centre. Journal of Large-Scale Research Facilities JLSRF **1**, A1 (2015). https://doi.org/10.17815/jlsrf-1-18
59. Yu, W., Vetter, J., Canon, R.S., Jiang, S.: Exploiting lustre file joining for effective collective IO. In: Seventh IEEE International Symposium on Cluster Computing and the Grid (CCGrid '07), pp. 267–274. IEEE (2007). https://doi.org/10.1109/CCGRID.2007.51
60. Liou, M.S., Steffen, C.J.: A new flux splitting scheme. J. Comput. Phys. **107**(1), 23 (1993). https://doi.org/10.1006/jcph.1993.1122
61. van Leer, B.: Towards the ultimate conservative difference scheme. V. A second-order sequel to Godunov's method. J. Comput. Phys. **32**(1), 101 (1979). https://doi.org/10.1016/0021-9991(79)90145-1
62. Choi, H., Moin, P.: Effects of the computational time step on numerical solutions of turbulent flow. J. Comput. Phys. **113**(1), 1 (1994). https://doi.org/10.1006/jcph.1994.1112
63. Saint-Vernant, B., Wantzel, L.: Mémoire et expérience sur l'écoulement déterminé par des différences de pressions considérables. Journal de l'École Polytechnique **H.27**, 85ff (1839)
64. Bhatnagar, P.L., Gross, E.P., Krook, M.: A model for collision processes in gases. I. Small amplitude processes in charged and neutral one-component systems. Phys. Rev. **94**(3), 511 (1954). https://doi.org/10.1103/PhysRev.94.511
65. Hänel, D.: Molekulare Gasdynamik, Einführung in die kinetische Theorie der Gase und Lattice-Boltzmann-Methoden. Springer, Berlin (2004)
66. Qian, Y.H., D'Humières, D., Lallemand, P.: Lattice BGK models for Navier-Stokes equation. Europhysics Letters (EPL) **17**(6), 479 (1992). https://doi.org/10.1209/0295-5075/17/6/001
67. Dupuis, A., Chopard, B.: Theory and applications of an alternative lattice Boltzmann grid refinement algorithm. Phys. Rev. E. **67**(6), 1 (2003). https://doi.org/10.1103/PhysRevE.67.066707
68. Bouzidi, M., Firdaouss, M., Lallemand, P.: Momentum transfer of a Boltzmann-lattice fluid with boundaries. Phys. Fluids **13**(11), 3452 (2001). https://doi.org/10.1063/1.1399290
69. Schreck, S., Sullivan, K.J., Ho, C.M., Chang, H.K.: Correlations between flow resistance and geometry in a model of the human nose. J. Appl. Physiol. (Bethesda, Md. : 1985) **75**(4), 1767 (1993)
70. Vogt, K., Hoffrichter, H.: Neue Strömungsphysikalische Erkenntnisse in der Rhinomanometrie und ihre praktischen Konsequenzen. In: Mösges, S. (ed.) Topische Therapie der allergischen Rhinitis, Biermann, Germany, pp. 45–60 (1993)
71. Benninger, M., Senior, B.: The development of the rhinosinusitis disability index. Arch. Otolaryngol. Head Neck Surg. **123**(11), 1175 (1997). https://doi.org/10.1001/archotol.1997.01900110025004